MNRAS 000, 1–20 (2017) Preprint 26 June 2018 Compiled using MNRAS LaTeX style file v3.0

Bow shocks, bow waves, and dust waves

William J. Henney, S. Jane Arthur, & Jorge A. Tarango-Yong
Instituto de Radioastronomía y Astrofísica, Universidad Nacional Autónoma de México, Apartado Postal 3-72, 58090 Morelia, Michoacán, México

Accepted XXX. Received YYY; in original form ZZZ

ABSTRACT
Dust waves and bow waves result from the action of a star's radiation pressure on a stream of dust grains that is flowing past it. They are an alternative mechanism to hydrodynamic bow shocks for explaining the curved arcs of infrared emission seen around some stars. We employ simple cylindrically symmetric models for the dust grain dynamics under the influence of radiation and weak gas–grain coupling, which produce bow shapes that we call dragoids. We also show how thin-shell hydrodynamic models can be modified to treat the case of strong gas-grain coupling, producing bow shapes that we call trapoids. Using our recently developed two-dimensional classification scheme for projected bow shapes, we then analyze the inclination-dependent tracks of the dragoids and trapoids in the planitude–alatude plane, finding interesting differences from the wilkinoid, cantoid, and ancantoid shapes of hydrodynamic bow shock models. We further show how these are modified in the presence of small-amplitude standing-wave oscillations of the basic shape, as may be produced by hydrodynamic instabilities or a time-varying source. We analyze the prospects of using shape analysis of observational datasets to discriminate between different bow models, finding that sample sizes of order 100 are required.

Key words: circumstellar matter – radiation: dynamics – stars: winds, outflows

1 INTRODUCTION

Curved emission arcs around stars (e.g., Gull & Sofia 1979) are often interpreted as *bow shocks*, due to a supersonic hydrodynamic interaction between the star's wind and an external stream. This stream may be due to the star's own motion or to an independent flow, such as an H ii region in the champagne phase (Tenorio-Tagle 1979), or another star's wind (Canto et al. 1996). However, an alternative interpretation in some cases may be a radiation-pressure driven bow wave, as first proposed by van Buren & McCray (1988, §vi). In this scenario, photons emitted by the star are absorbed by dust grains in the incoming stream, with the resultant momentum transfer being sufficient to decelerate and deflect the grains within a certain distance from the star, forming a dust-free, bow-shaped cavity with an enhanced dust density at its edge. Two regimes are possible, depending on the strength of coupling between the gas (or plasma) and the dust. In the strong-coupling regime, gas–grain drag decelerates the gas along with the dust, forming a shocked gas shell in a similar fashion to the wind-driven bow shock case. In the weak-coupling regime, the gas stream is relatively unaffected and the dust temporarily decouples to form a dust-only shell. This second case has recently been studied in detail in the context of the interaction of late O-type stars (which have only weak stellar winds) with dusty photoevaporation flows inside H ii regions (Ochsendorf et al. 2014b,a; Ochsendorf & Tielens 2015). We follow the nomenclature proposed by Ochsendorf et al. (2014a), in which *dust wave* refers to the weak coupling case and *bow wave* to the strong coupling case. More complex, hybrid scenarios are also possible, such as that studied by van Marle et al. (2011), where a hydrodynamic bow shock forms, but the larger dust grains that accompany the stellar wind pass right through the shocked gas shell, and form their own dust wave at a larger radius.

In Tarango Yong & Henney (2018, hereafter Paper I), we proposed a new two-dimensional classification scheme for bow shapes: the projected planitude–alatude, or Π'–Λ', diagram. Planitude measures the flatness of the bow's apex, while alatude measures the openness of the bow's wings. Both are dimensionless ratios of lengths that can be estimated from observational images. We have analyzed the inclination-dependent tracks on the Π'–Λ' plane for simple geometric shapes (spheroids, paraboloids, hyperboloids) and for thin-shell hydrodynamic bow shock models (wilkinoid, cantoids, ancantoids). In this paper, we will do the same for simple models of radiation-driven dust waves (dragoids) and bow waves (trapoids).

The paper is organized as follows. In § **??** we do the same for simple models of a dusty radiation bow wave (dragoids), including the effects of gas-grain drag. In § **??** we investigate the effects on the planitude–alatude plane of small-amplitude perturbations to the bow shape.

2 DIFFERENT TYPES OF BOW

In this section, we investigate the different types of bow interaction that will occur in different regions of parameter space. We will

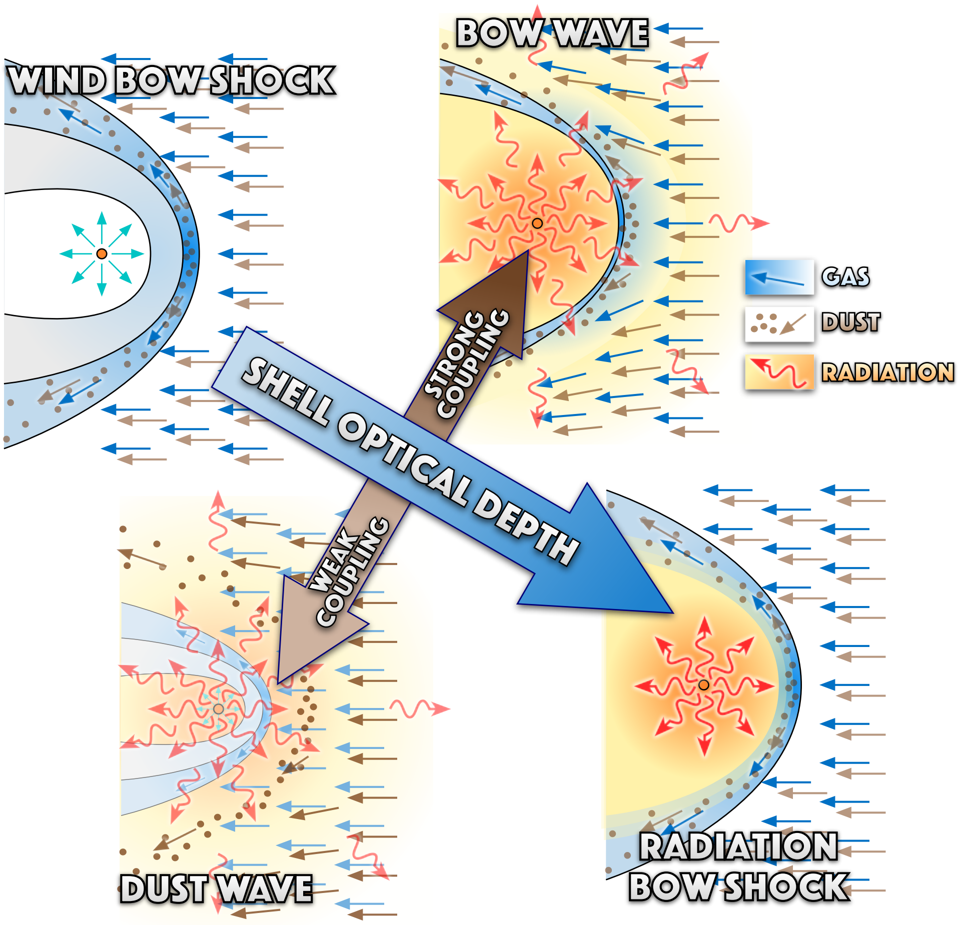

Figure 1. Bow shocks, bow waves, and dust waves

mainly treat the canonical case[1] of a bow around a star of bolometric luminosity, L, with a radiatively driven wind, which is immersed in an external stream of gas and dust with density, ρ, and velocity, v. The size and shape of the bow is determined by a generalized balance of pressure (or, equivalently, momentum) between internal and external sources. We assume that the stream is supersonic and super-alfvenic, so that the external pressure is dominated by the ram pressure: ρv^2.

2.1 Strong gas-grain coupling

We first consider the case where the dust grains and gas are perfectly coupled by collisions.[2] Although dust grains typically constitute only a small fraction $Z_d \sim 0.01$ of the mass of the external stream, they nevertheless dominate the broad-band opacity at FUV, optical and IR wavelengths if they are present.[3] The strong coupling assumption means that all the radiative forces applied to the dust grains are directly felt by the gas also.

2.1.1 *Bows supported by radiation and wind*

The internal pressure is the sum of wind ram pressure and the effective radiation pressure that acts on the bow shell. The radiative momentum loss rate of the star is L/c and the wind momentum loss rate can be expressed as

$$\dot{M}V = \eta L/c\,, \tag{1}$$

where η is the momentum efficiency of the wind, which is typically < 1 (Lamers & Cassinelli 1999). If the optical depth is very large, then all of the stellar radiative momentum, emitted with rate L/c,

[1] Variant cases with differing arrangements of dust and radiation sources are treated in § 4.1.
[2] Cases where this assumption does not hold are investigated below in § 2.2.
[3] At EUV wavelengths ($\lambda < 912$ Å), gas opacity dominates if the hydrogen neutral fraction is larger than ≈ 0.001, see discussion of ionization front trapping below.

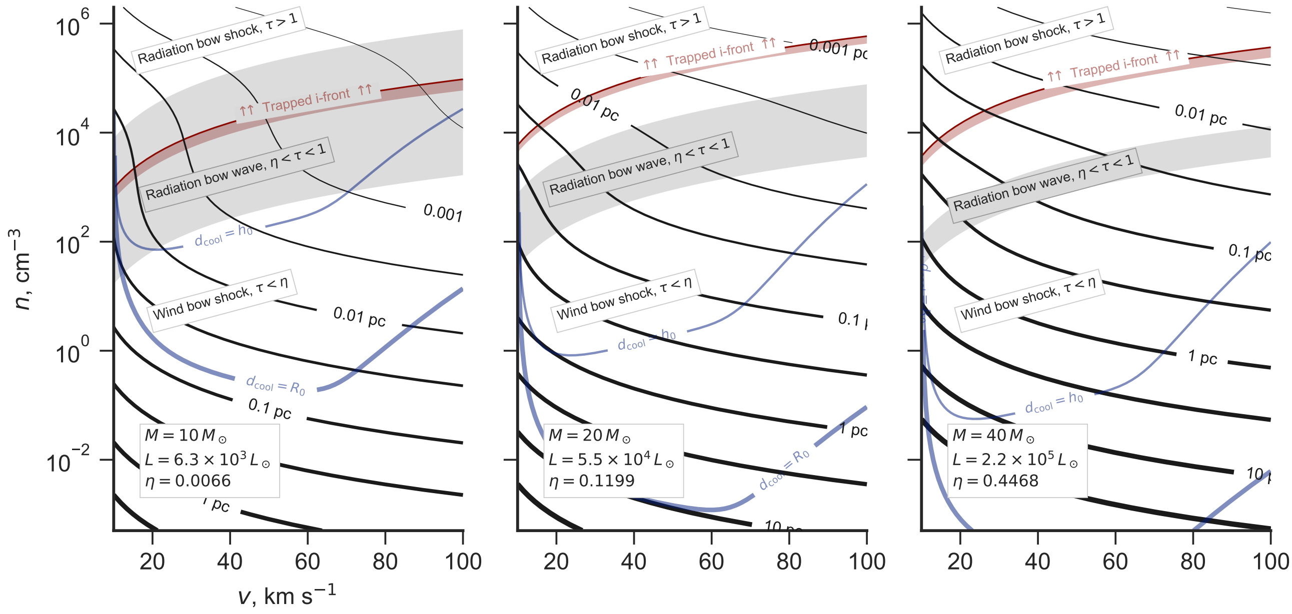

Figure 2. Bow regimes in parameter space (v, n) of the external stream for main-sequence OB stars of different masses: (a) $10\,\mathrm{M}_\odot$, (b) $20\,\mathrm{M}_\odot$, (c) $40\,\mathrm{M}_\odot$. In all cases, $\kappa = 600\,\mathrm{cm}^2\,\mathrm{g}^{-1}$ and efficient gas-grain coupling is assumed. Solid black lines of varying width show the bow size (star-apex separation, R_0), while gray shading shows the radiation bow wave regime, with lower border $\tau = \eta$ and upper border $\tau = 1$, where $\tau = 2\kappa\rho R_0$ is the optical depth through the bow. For bows above the red solid line, the ionization front is trapped inside the bow. Blue lines delineate different cooling regimes. Above the thin blue line ($d_{\mathrm{cool}} = h_0$), the bow shock radiates efficiently, forming a thin shocked shell. Below the thick blue line ($d_{\mathrm{cool}} = R_0$), the bow shock is essentially non-radiative.

is trapped by the bow shell. In the single scattering limit,[4] and temporarily neglecting the wind, then pressure balance at the bow apex, a distance R_0 along the symmetry axis from the star is given by

$$\frac{L}{4\pi c R_0^2} = \rho v^2 , \tag{2}$$

which yields a fiducial bow shock radius in this optically thick limit as

$$R_* = \left(\frac{L}{4\pi c \rho v^2} \right)^{1/2} . \tag{3}$$

We now consider the opposite, optically thin limit. If the total opacity (gas plus dust) per total mass (gas plus dust) is κ (with units of $\mathrm{cm}^2\,\mathrm{g}^{-1}$), then the radiative acceleration is

$$a_{\mathrm{rad}} = \frac{\kappa L}{4\pi c R^2} . \tag{4}$$

Therefore, an incoming stream with initial velocity, v_∞, can be brought to rest by radiation alone[5] at a distance R_{**} where

$$\int_{R_{**}}^{\infty} a_{\mathrm{rad}}\, dr = \tfrac{1}{2} v_\infty^2 , \tag{5}$$

yielding

$$R_{**} = \frac{\kappa L}{2\pi c v_\infty^2} . \tag{6}$$

On the other hand, we can also argue as in the optically thick case above by approximating the bow shell as a surface, and balancing stellar radiation pressure against the ram pressure of the incoming stream. The important difference when the shell is not optically thick is that only a fraction $1 - e^{-\tau}$ of the radiative momentum is absorbed by the bow, so that equation (2) is replaced with

$$\frac{L(1 - e^{-\tau})}{4\pi c R_0^2} = \rho v^2 . \tag{7}$$

In the optically thin limit, $1 - e^{-\tau} \approx \tau$, so these two descriptions can be seen to agree ($R_0 \to R_{**}$) so long as

$$\tau = 2\kappa\rho R_0 , \tag{8}$$

which we will assume to hold generally.

Then, defining a fiducial optical depth,

$$\tau_* = \rho\kappa R_* , \tag{9}$$

[4] Although it may seem inconsistent to assume single scattering in the case of high optical depths, this is defensible for the following reasons. (1) The grain albedo is not that high (typically ~ 0.5 at ultraviolet through optical wavelengths). (2) The scattered radiation field is more isotropic than the stellar field, leading to cancellation in the radiative flux. (3) Absorbed radiation is re-emitted at infrared wavelengths, where the dust opacity is very much lower.

[5] For simplicity, we here ignore the effects of gravity, which are important for low ratios of $\kappa L/M$, see § 2.1.2. We also ignore pressure gradients and shocks, which are important as the velocity approaches the sound speed, c_{s} (in § XX below, we show that the resultant corrections to R_0 are of order c_{s}/v_∞).

and adding in the stellar wind ram pressure[6] from equation (1), we find that the general bow radius can be written in terms of the fiducial radius as

$$R_0 = x R_* \,, \tag{10}$$

where x is the solution of

$$x^2 - \left(1 - e^{-2\tau_* x}\right) - \eta = 0 \,. \tag{11}$$

Since this is a transcendental equation, x must be found numerically, but we can write explicit expressions for three limiting cases:

$$x \approx \begin{cases} \text{if } \tau_* \gg 1: & (1+\eta)^{1/2} \\ \text{if } \tau_*^2 \ll 1: & \tau_* + \left(\tau_*^2 + \eta\right)^{1/2} \approx \begin{cases} \text{if } \tau_*^2 \gg \eta: & 2\tau_* \\ \text{if } \tau_*^2 \ll \eta: & \eta^{1/2} \end{cases} \end{cases} \tag{12}$$

The first case, $x \approx (1+\eta)^{1/2}$, corresponds to a *radiation bow shock*; the second case, $x \approx 2\tau_*$, corresponds to a *radiation bow wave*; and the third case, $x \approx \eta^{1/2}$, corresponds to a *wind bow shock*. The two bow shock cases are similar in that the external stream is oblivious to the presence of the star until it suddenly hits the bow shock shell, differing only in whether it is radiation or wind that is providing the internal pressure. In the intermediate bow wave case, on the other hand, the external stream is gradually decelerated by absorption of photons as it approaches the bow.[7]

We now consider the application to bow shocks around main sequence OB stars, expressing stellar and ambient parameters in terms of typical values as follows:

$$\begin{aligned} \dot{M}_{-7} &= \dot{M} / \left(10^{-7}\,\mathrm{M}_\odot\,\mathrm{yr}^{-1}\right) \\ V_3 &= V / \left(1000\,\mathrm{km\,s^{-1}}\right) \\ L_4 &= L / \left(10^4\,\mathrm{L}_\odot\right) \\ \upsilon_{10} &= \upsilon_\infty / \left(10\,\mathrm{km\,s^{-1}}\right) \\ n &= (\rho/\bar{m}) / \left(1\,\mathrm{cm^{-3}}\right) \\ \kappa_{600} &= \kappa / \left(600\,\mathrm{cm^2\,g^{-1}}\right) , \end{aligned}$$

where $\bar{m}$ is the mean mass per hydrogen nucleon ($\bar{m} \approx 1.3 m_\mathrm{p} \approx 2.17 \times 10^{-24}$ g for solar abundances). Note that $\kappa = 600\,\mathrm{cm^2\,g^{-1}}$ corresponds to a cross section of $\approx 10^{-21}\,\mathrm{cm^2}$ per hydrogen nucleon, which is typical for interstellar medium dust (Bertoldi & Draine 1996) at far ultraviolet wavelengths, where OB stars emit most of their radiation. In terms of these parameters, we can express the stellar wind momentum efficiency as

$$\eta = 0.495\, \dot{M}_{-7}\, V_3\, L_4^{-1} \tag{13}$$

and the fiducial radius and optical depth as

$$R_*/\mathrm{pc} = 2.21\, (L_4/n)^{1/2}\, \upsilon_{10}^{-1} \tag{14}$$

$$\tau_* = 0.0089\, \kappa_{600}\, (L_4\, n)^{1/2}\, \upsilon_{10}^{-1} \,. \tag{15}$$

In Figure 2, we show results for the bow size (apex distance, R_0) as a function of the density, n, and relative velocity, υ_∞, of the external stream, with each panel corresponding to a particular star, with parameters as shown in Table 1. To facilitate comparison with previous work, we choose stellar parameters similar to those used in

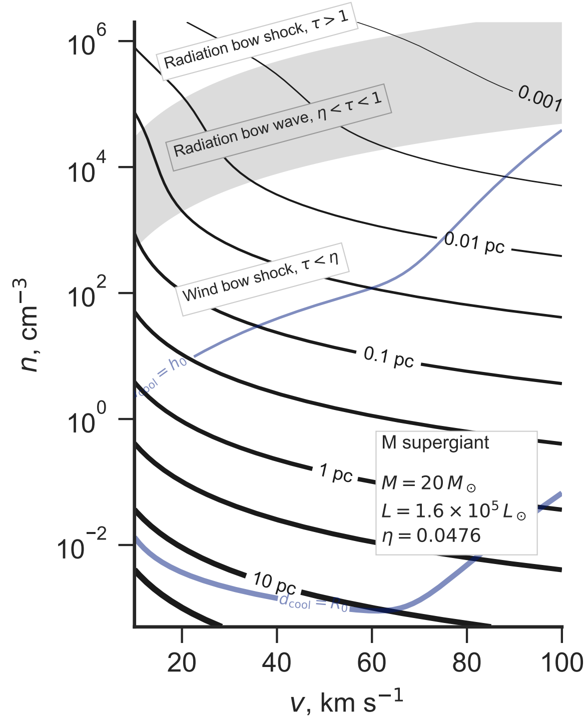

Figure 3. As Fig. 2, but for a cool M-type supergiant instead of hot main sequence stars. A smaller dust opacity is used, $\kappa = 60\,\mathrm{cm^2\,g^{-1}}$, because of the reduced extinction efficiency at the optical/infrared wavelengths emitted by this star.

the hydrodynamical simulations of Meyer et al. (2014, 2016, 2017), based on stellar evolution tracks for stars of $10\,\mathrm{M}_\odot$, $20\,\mathrm{M}_\odot$ and $40\,\mathrm{M}_\odot$ (Brott et al. 2011) and theoretical wind prescriptions (de Jager et al. 1988; Vink et al. 2000). Although the stellar parameters do evolve with time, they change relatively little during the main-sequence lifetime of several million years.[8] The three examples are an early B star ($10\,\mathrm{M}_\odot$), a late O star ($20\,\mathrm{M}_\odot$), and an early O star ($40\,\mathrm{M}_\odot$), which cover the range of luminosities and wind strengths expected from bow-producing hot main sequence stars. The luminosity is a steep function of stellar mass ($L \sim M^{2.5}$) and the wind mass-loss rate is a steep function of luminosity ($\dot{M} \sim L^{2.2}$), which means that the wind momentum efficiency is also a steep function of mass ($\eta \sim M^3$), approaching unity for early O stars, but falling to less than 1% for B stars.

[6] We implicitly assume that the interaction of the stellar wind with the external stream can always be treated in the continuum limit. This will be true if either the collisional mean free path or the ion Larmor radius is much smaller than R_0, which is almost always the case.

[7] A shock does still form in this case, but shocked material constitutes only a fraction of the total column density of the shell, see § **??**.

[8] Note that we have recalculated the stellar wind terminal velocities, since the values given in the Meyer et al. papers are troublingly low. We have used the prescription $V = 2.6 V_\mathrm{esc}$, where $V_\mathrm{esc} = (2GM(1-\Gamma_e)/R)^{1/2}$ is the photospheric escape velocity, which is appropriate for strong line-driven winds with $T_\mathrm{eff} > 21\,000$ K (Lamers et al. 1995). We find velocities of $2500\,\mathrm{km\,s^{-1}}$ to $3300\,\mathrm{km\,s^{-1}}$, which are consistent with observations and theory (Vink et al. 1999) for O stars, but at least two times higher than those cited by Meyer et al. (2014). For main-sequence B stars, wind column densities are too low to reliably measure the terminal velocity from near ultraviolet P Cygni profiles (Prinja 1989), and so the values are theory-dependent (Krtička 2014) and hence more uncertain. A further complication is the existence of a subset of OB stars with anomalously weak winds (Puls et al. 2008), which in some cases is related to the presence of strong ($\sim$ 1 kG) magnetic fields (Oskinova et al. 2011).

Table 1. Stellar parameters for example stars

	$M/\mathrm{M}_\odot$	L_4	$\dot{M}_{-7}$	V_3	η	Sp. Type	T_eff/kK	λ_eff / µm	S_{49}	Figures
	10	0.63	0.0034	2.47	0.0066	B1.5 V	25.2	0.115	0.000 13	2a, ??, ??
Main-sequence OB stars	20	5.45	0.492	2.66	0.1199	O9 V	33.9	0.086	0.16	2b
	40	22.2	5.1	3.31	0.4468	O5 V	42.5	0.068	1.41	2c
Blue supergiant star	33	30.2	20.2	0.93	0.3079	B0.7 Ia	23.5	0.123	0.016	4
Red supergiant star	20	15.6	100	0.015	0.0476	M1 Ia	3.6	0.805	0	3

It can be seen from Figure 2 that the onset of the radiation bow wave regime is very similar for the three main-sequence stars, occurring at $n > 20$ to $40\, v_{10}^2$. An important difference, however, is that for the $40\,\mathrm{M}_\odot$ star, which has a powerful wind, the radiation bow wave regime only occurs for a very narrow range of densities, whereas for the $10\,\mathrm{M}_\odot$ star, with a much weaker wind, the regime is much broader, extending to $n < 10^4\, v_{10}^2$. Another difference is the size scale of the bows in this regime, which is $R_0 = 0.001$ pc to 0.003 pc for the $10\,\mathrm{M}_\odot$ star if $v_\infty = 40\,\mathrm{km\,s^{-1}}$, but $R_0 \approx 0.1$ pc for the $40\,\mathrm{M}_\odot$ star, assuming the same inflow velocity.

Figure 3 shows results for a cool M-type super-giant star with stellar parameters inspired by Betelgeuse (α Orionis), as listed in Table 1. Unlike the UV-dominated spectrum of the hot stars, this star emits predominantly in the near-infrared, where the dust extinction efficiency is lower, so we adopt a lower opacity of $60\,\mathrm{cm^2\,g^{-1}}$. This has the effect of shifting the radiation bow wave regime to higher densities: $n = 1000$ to $30\,000\, v_{10}^2$ in this case.

2.1.2 *Effects of stellar gravity*

In principle, gravitational attraction from the star, of mass M, will partially counteract the radiative acceleration. This can be accounted for by replacing L with an effective luminosity

$$L_\mathrm{eff} = L\left(1 - \Gamma_\mathrm{E}^{-1}\right), \tag{16}$$

in which Γ_E is the Eddington factor:

$$\Gamma_\mathrm{E} = \frac{\kappa L}{4\pi c G M} = 458.5\,\frac{\kappa_{600} L_4}{M}, \tag{17}$$

where, in the last expression, M is measured in solar masses. For the stars in Table 1, we find $\Gamma_\mathrm{E} \approx 30$ to 400, so gravity can be safely ignored. The only exception is when the optical depth of the bow is very large: $\tau > \ln \Gamma_\mathrm{E} \sim 5$, in which case gravity may be important in the outer parts of the shell (see Rodríguez-Ramírez & Raga 2016).

2.1.3 *Ionization state of the bow shell*

In this section we calculate whether the star is capable of photoionizing the entire bow shock shell, or whether the ionization front will be trapped within it. The number of hydrogen recombinations[9] per unit time per unit area in a fully ionized shell is

$$\mathcal{R} = \alpha_\mathrm{B} n_\mathrm{sh}^2 h_\mathrm{sh}, \tag{18}$$

while the advective flux of hydrogen nuclei through the shock is

$$\mathcal{A} = n v, \tag{19}$$

[9] The diffuse field is treated in the on-the-spot approximation, assuming all emitted Lyman continuum photons are immediately re-absorbed locally, so the case B recombination co-efficient, $\alpha_\mathrm{B} = 2.6\times10^{-13}\,T_4^{-0.7}\,\mathrm{cm^3\,s^{-1}}$, is used, where $T_4 = T/10^4$ K.

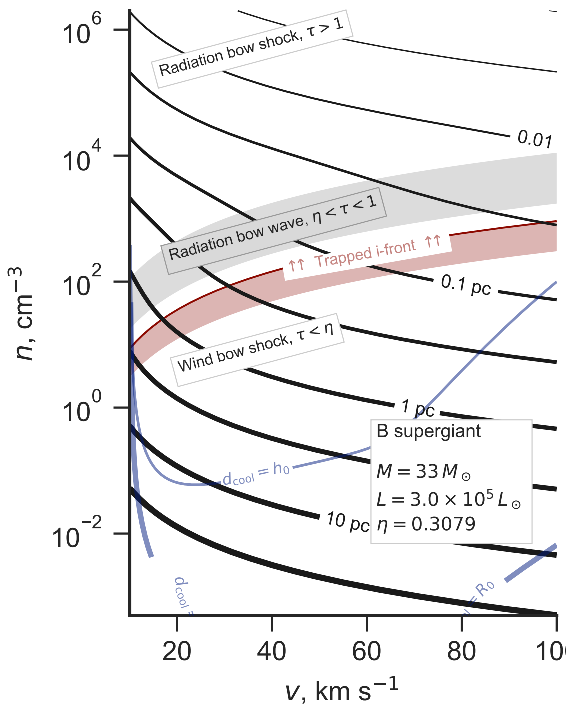

Figure 4. As Fig. 2, but for an evolved B-type supergiant instead of main sequence stars. This is similar to the early O MS star of Fig. 2c in many respects, except for the trapping of the ionization front, which occurs for much lower outer stream densities.

and the flux of hydrogen-ionizing photons ($h\nu > 13.6$ eV) incident on the inner edge of the shell is

$$\mathcal{F} = \frac{S}{4\pi R_0^2}, \tag{20}$$

where S is the ionizing photon luminosity of the star. Any shell with $\mathcal{R} + \mathcal{A} > \mathcal{F}$ cannot be entirely photoionized by the star, and so must have trapped the ionization front.

The ratio of advective particle flux to ionizing flux is, from equations (3), (19), (20),

$$\frac{\mathcal{A}}{\mathcal{F}} = 5.86\times10^{-5}\,\frac{x^2 L_4}{v_{10} S_{49}}, \tag{21}$$

which is nearly always small. For clarity of exposition, we therefore ignore $\mathcal{A}$ in the following discussion, although it is included in quantitative calculations. The column density of the shocked shell can be found, for example, from equations (10) and (12) of Wilkin (1996) in the limit $v_\infty/V \to 0$ (Wilkin's parameter α) and $\theta \to 0$.

This yields

$$n_{\rm sh} h_{\rm sh} = \tfrac{3}{4} n R_0 \,. \tag{22}$$

Assuming strong cooling behind the shock,[10] the shell density is

$$n_{\rm sh} = \mathcal{M}_0^2 n \tag{23}$$

where $\mathcal{M}_0 = v_\infty / c_{\rm s}$ is the isothermal Mach number of the external stream.[11] Putting these together with equations (3) and (9), one finds that $\mathcal{R} > \mathcal{F}$ implies

$$x^3 \tau_* > \frac{4 S c c_{\rm s} \bar{m}^2 \kappa}{3 \alpha L} \,. \tag{24}$$

From equation (11), it can be seen that x depends on the external stream parameters, n, v_∞ only via τ_*, and so equation (24) is a condition for τ_*, which, by using equation (15), becomes a condition on n/v_{10}^2. In the radiation bow shock case, $x = (1+\eta)^{1/2}$, and the condition can be written:

$$\frac{n}{v_{10}^2} > 2.65 \times 10^8 \, \frac{S_{49}^2 T_4^{3.4}}{L_4^3 (1+\eta)^3} \,, \tag{25}$$

where

$$S_{49} = S / \left(10^{49}\ {\rm s^{-1}}\right) \,.$$

Numerical values of S_{49} for our three example stars are given in Table 1, taken from Figure 4 of Sternberg et al. (2003). In the radiation bow wave case, $x = 2\tau_*$, and the condition can be written:

$$\frac{n}{v_{10}^2} > 5.36 \times 10^4 \, \frac{S_{49}^{1/2} T_4^{0.85}}{\kappa_{600}^{3/2} L_4^{3/2}} \,. \tag{26}$$

In the wind bow shock case, the result is the same as equation (25), but changing the factor $(1+\eta)^3$ to η^3. For the example hot stars in Table 1, and assuming $\kappa_{600} = 1$, $T_4 = 0.8$, the resulting density threshold is $n > (1000 \text{ to } 5000)\, v_{10}^2$, depending only weakly on the stellar parameters, which is shown by the red lines in Figure 2. For the $10\,{\rm M_\odot}$ star, this is in the radiation bow wave regime, whereas for the higher mass stars it is in the radiation bow shock regime. When the external stream is denser than this, then the outer parts of the shocked shell may be neutral instead of ionized, giving rise to a cometary compact H II region (Mac Low et al. 1991; Arthur & Hoare 2006). This is only necessarily true, however, when the star is isolated. If the star is in a cluster environment, then the contribution of other nearby massive stars to the ionizing radiation field must be considered.

Quite different results are obtained for a B-type supergiant star (see Tab. 1 and Fig. 4), which has a similar bolometric luminosity and wind strength to the $40\,{\rm M_\odot}$ main-sequence star, but a hundred times lower ionizing luminosity. This results in a far lower threshold for trapping the ionization front of $n > 40 v_{10}^2$. The advective flux, $\mathcal{A}$, is relatively stronger for this star than for the main-sequence stars, but even for $v_{10} < 2$, where the effect is strongest, the change is only of order the width of the dark red line in Figure 4.

In principle, when the ionization front trapping occurs in the bow wave regime, then the curves for R_0 will be modified in the region above the red line because all of the ionizing radiation is trapped in the shell due to gas opacity, which is not included in equation (8). However, this only happens for our $10\,{\rm M_\odot}$ star, which has a relatively soft spectrum. Table 1 gives the peak wavelength of the stellar spectrum for this star as $\lambda_{\rm eff} = 0.115\,\mu{\rm m}$, which is significantly larger than the hydrogen ionization threshold at $0.0912\,\mu{\rm m}$, meaning that only a small fraction of the total stellar luminosity is in the EUV band and affected by the gas opacity. The effect on R_0 is therefore small. For the higher mass stars, $\lambda_{\rm eff} < 0.0912\,\mu{\rm m}$, so the majority of the luminosity is in the EUV band, but in these cases the ionization front trapping occurs well inside the radiation bow shock zone, where the dust optical depth is already sufficient to trap all of the radiative momentum.

2.1.4 *Radiative cooling lengths*

In this section, we calculate whether the radiative cooling is sufficiently rapid behind the bow shock to allow the formation of a thin, dense shell. Since cooling is least efficient at low densities, we will assume that the wind bow shock regime applies unless otherwise specified. We label quantities just outside the shock by the subscript "0", quantities just inside the shock (after thermalization, but before any radiative cooling) by the subscript "1", and quantities after the gas has cooled back to the photoionization equilibrium temperature by the subscript "2". Assuming a ratio of specific heats, $\gamma = 5/3$, the relation between the pre-shock and immediate post-shock quantities is

$$\frac{n_1}{n_0} = \frac{4\mathcal{M}_0^2}{\mathcal{M}_0^2 + 3} \tag{27}$$

$$\frac{T_1}{T_0} = \tfrac{1}{16}\left(5\mathcal{M}_0^2 - 1\right)\left(1 + 3/\mathcal{M}_0^2\right) \tag{28}$$

$$\frac{v_1}{v_0} = \left(\frac{n_1}{n_0}\right)^{-1} \,, \tag{29}$$

where $\mathcal{M}_0 = v_0 / c_{\rm s}$. The cooling length of the post-shock gas can be written as

$$d_{\rm cool} = \frac{3 P_1 v_1}{2(\mathcal{L}_1 - \mathcal{G}_1)} \,, \tag{30}$$

where P_1 is the thermal pressure and $\mathcal{L}_1$, $\mathcal{G}_1$ are the volumetric radiative cooling and heating rates. For fully photoionized gas, we have $P_1 \approx 2 n_1 k T_1$, $\mathcal{L}_1 = n_1^2 \Lambda(T_1)$, and $\mathcal{G}_1 = n_1^2 \Gamma(T_1)$, where $\Lambda(T)$ is the cooling coefficient, which is dominated by metal emission lines that are excited by electron collisions, and $\Gamma(T)$ is the heating coefficient, which is dominated by hydrogen photo-electrons (Osterbrock & Ferland 2006). The cooling coefficient has a maximum around 10^5 K, and for typical ISM abundances can be approximated as follows:

$$\Lambda_{\rm warm} = 3.3 \times 10^{-24}\, T_4^{2.3}\ {\rm erg\,cm^{-3}\,s^{-1}} \tag{31}$$

$$\Lambda_{\rm hot} = 10^{-20}\, T_4^{-1}\ {\rm erg\,cm^{-3}\,s^{-1}} \tag{32}$$

$$\Lambda = \left(\Lambda_{\rm warm}^{-k} + \Lambda_{\rm hot}^{-k}\right)^{-1/k} \quad \text{with} \quad k = 3 \,, \tag{33}$$

which is valid in the range $0.7 < T_4 < 1000$. We approximate the heating coefficient as

$$\Gamma = 1.77 \times 10^{-24}\, T_4^{-1/2}\ {\rm erg\,cm^{-3}\,s^{-1}} \,, \tag{34}$$

where the coefficient is chosen so as to give $\Gamma = \Lambda$ at an equilibrium temperature of $T_4 = 0.8$.

In Figure 2 we show curves calculated from equations (27)

[10] This is shown to be justified in § 2.1.4.

[11] The sound speed depends on the temperature and hydrogen and helium ionization fractions, y and $y_{\rm He}$ as $c_{\rm s}^2 = (1 + y + z_{\rm He} y_{\rm He})(kT/\bar{m})$, where $z_{\rm He}$ is the helium nucleon abundance by number relative to hydrogen and $k = 1.380\,650\,3 \times 10^{-16}\ {\rm erg\,K^{-1}}$ is Boltzmann's constant. We assume $y = 1$, $y_{\rm He} = 0.5$, $z_{\rm He} = 0.09$, so that $c_{\rm s} = 11.4\, T_4^{1/2}\ {\rm km\,s^{-1}}$.

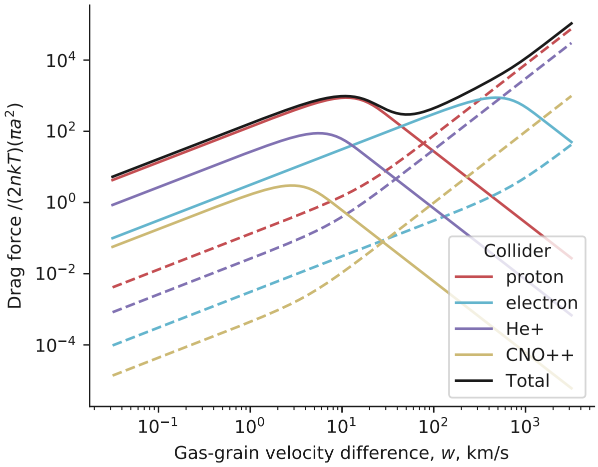

Figure 5. Contributions of different collider species to the dimensionless drag force, $f_{\rm drag}/f_*$, as a function of gas–grain slip velocity, w. Solid lines show the Coulomb (electrostatic) drag, while dashed lines show the Epstein (solid-body) drag. Results are shown for dimensionless grain potential $\phi = 10$. All Coulomb forces scale with ϕ^2, while the Epstein forces are independent of ϕ. The species labelled "CNO++" represents the combined effect of all metals (see footnote 14).

to (34), corresponding to $d_{\rm cool} = R_0$ (thick blue line) and $d_{\rm cool} = h_0$ (thin blue line), where h_0 is the shell thickness in the efficient cooling case. In this context, $n_0 = n$ and $n_2 = n_{\rm sh}$, so that h_0 follows from equations (22) and (23) as

$$h_0 = \tfrac{3}{4}\mathcal{M}_0^{-2} R_0 \, . \tag{35}$$

The bends in the curves at $v \approx 50\,{\rm km\,s^{-1}}$ are due to the maximum in the cooling coefficient $\Lambda(T)$ around 10^5 K. For bows with outer stream densities above the thin blue line, radiative cooling is so efficient that the bow shock can be considered isothermal, and so the shell is dense and thin (at least, in the apex region). It can be seen that the ionization front trapping always occurs at densities larger than this, which justifies the use of equation (23) in the previous section. For bows with outer stream densities below the thick blue line, cooling is unimportant and the bow shock can be considered non-radiative. In this case the shell is thicker than in the radiative case, $h_{\rm sh}/R_0 \approx 0.2$ to 0.3.[12] For bows with outer stream densities between the two blue lines, cooling does occur, albeit inefficiently, so that the shell thickness is set by $d_{\rm cool}$ rather than h_0.

2.2 Imperfect coupling between gas and dust

If the radiation field is sufficiently strong, then the collisional coupling between grains and gas will break down. In this section, we calculate the regions of star+stream parameter space where this might occur, leading to a separation of the bow into an outer dust wave and an inner, dust-free bow shock.

[12] An approximate value can be found from equation (22) by substituting $n = n_0$ and $n_{\rm sh} \approx n_1$, then using equation (27). Consideration of the slight increase in density between the shock and the contact discontinuity reduces this value by 5–10%.

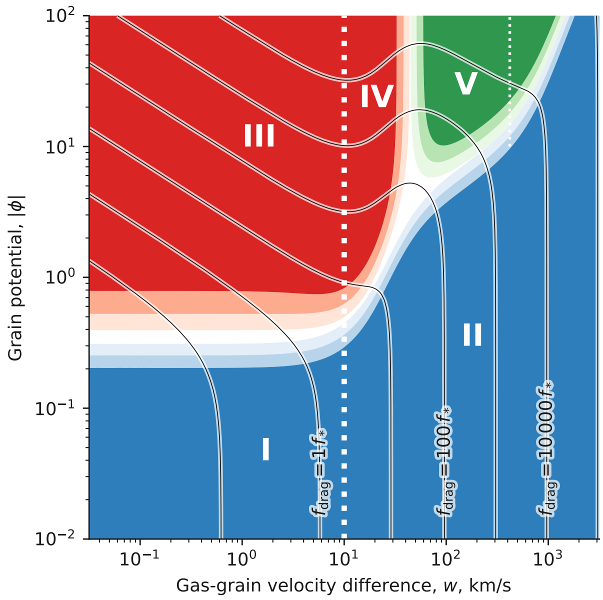

Figure 6. Regimes of gas–grain drag as a function of slip velocity and grain potential. The different regimes are indicated by bold roman numerals, as explained in Table 2. Blue shading indicates regions dominated by Epstein (solid-body) drag, whereas red and green shading indicate regions dominated by Coulomb drag due to protons and electrons, respectively. In each case, the saturated color represents a contribution > 70% of the relevant component to the total drag force, while progressively lighter shading represents the > 60% and > 50% levels. The thick white dotted line indicates the transition between the subthermal and superthermal regimes for protons, while the thin white dotted line indicates the corresponding transition for electrons. Contours show the total drag force in units of f_* (see eq. [37]) in decade intervals from 0.1 to 10^4, as labelled. Results are shown for $T = 8000$ K and $n = 100\,{\rm cm^{-3}}$, but the differences are very slight throughout the ranges $T = 5000$ K to 15 000 K and $n = 10^{-3}\,{\rm cm^{-3}}$ to $10^6\,{\rm cm^{-3}}$.

Table 2. Regimes of drag force as function of grain potential and slip speed

	Regime	Approximate criteria	$f_{\rm drag}/f_*$
I	Epstein subsonic	$\phi^2 \ll 1$ and $w_{10} < 1$	$1.5\, w_{10}$
II	Epstein supersonic	$w_{10} > 1$ and $w_{10} > 5\,\lvert\phi\rvert$	w_{10}^2
III	Coulomb p$^+$ subthermal	$\phi^2 > 1$ and $w_{10} < 1$	$(1 + 20\,\phi^2)\, w_{10}$
IV	Coulomb p$^+$ superthermal	$\phi^2 > 1$ and $1 < w_{10} < 5$	$w_{10}^2 + 10\,\phi^2/w_{10}^2$
V	Coulomb e$^-$ subthermal	$\phi^2 > 20$ and $5 < w_{10} < 42$	$0.48\,\phi^2\, w_{10}$

2.2.1 *Drag force on grains*

The drag force on a charged dust grain moving at a relative speed w through a plasma has contributions from both direct collisions and from electrostatic Coulomb interactions with ions and electrons. We use the expressions in Draine & Salpeter (1979), equations (4)–(6), considering the contributions from protons, electrons, helium

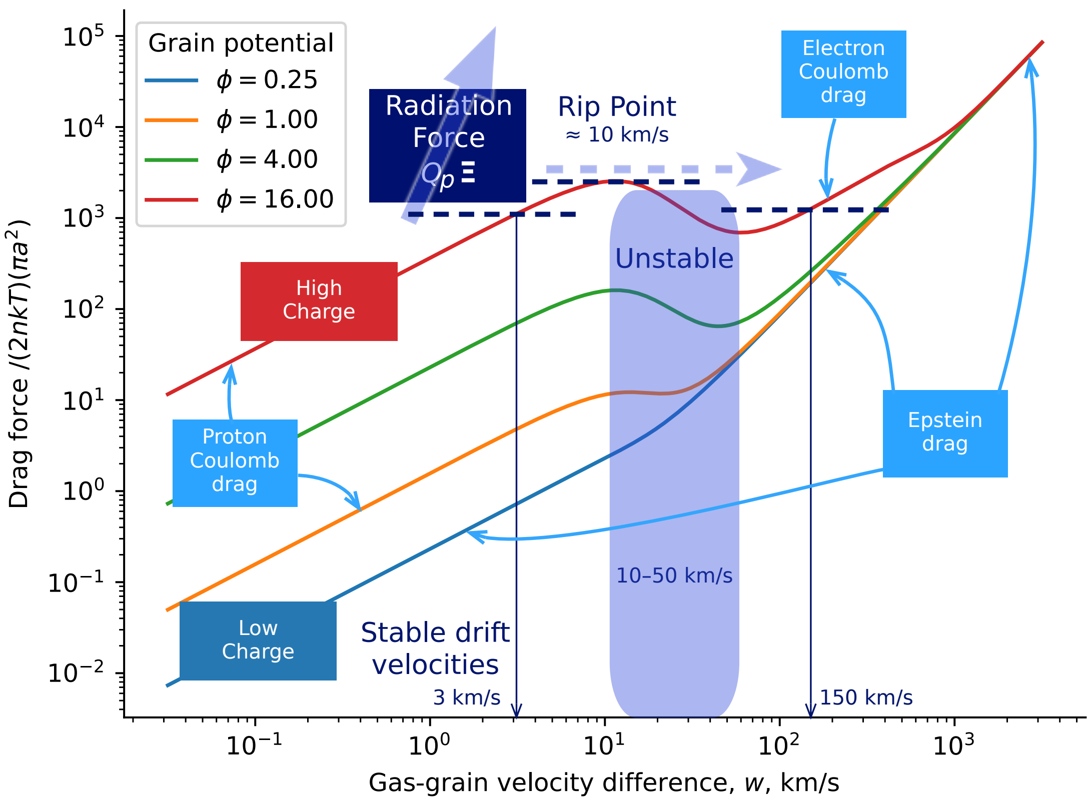

Figure 7. Dimensionless drag force, $f_{\rm drag}/f_*$, as a function of gas–grain slip velocity, w, for different values of the grain potential in thermal units, ϕ. Contributions from proton and electron Coulomb (electrostatic) drag, as well as Epstein (solid-body) drag are indicated. Examples of subsonic and highly supersonic stable drift velocities are shown (thin dark blue arrows), where the drag force is in equilibrium with the radiation force (thick dark blue dashed lines), while blue shading indicates the unstable, mildly supersonic velocity regime, where no stable drift equilibrium exists. Inset graph shows ϕ as a function of the radiation parameter, $\Xi = P_{\rm rad}/P_{\rm gas}$ on a log–linear scale for a collection of Cloudy models (see Appendix A).

ions,[13] and metal ions.[14] Results are shown in Figure 5, where dashed lines correspond to direct solid body collisions and solid lines to electrostatic interactions. The latter depend on the grain potential, which is described in dimensionless terms by ϕ, which is the electrostatic potential energy of a unit charge at the surface of a grain of charge $z_{\rm d}$ and radius a, in units of the characteristic thermal energy of a gas particle:

$$\phi = \frac{e^2 z_{\rm d}}{akT} \,. \tag{36}$$

The electrostatic contributions to $f_{\rm drag}$ are proportional to ϕ^2 (results are shown for $|\phi| = 10$), whereas the solid-body contributions are independent of ϕ. The drag force is put in dimensionless units by dividing by a characteristic force:

$$f_* = 2nkT \cdot \pi a^2 \,, \tag{37}$$

which is approximately[15] the ionized gas pressure multiplied by the grain geometric cross section.

For grains with low electric charge, $\phi^2 \ll 1$, the drag force is dominated by direct collisions of protons with the grain (dashed red line in Fig. 5). The gas collisional mean free path is much larger than the grain size, so the drag is in the Epstein regime (Weidenschilling 1977). As the relative gas–grain slip speed, w, increases, $f_{\rm drag}$ first increases linearly with w reaching $f_{\rm drag} \approx f_*$ at $w = c_{\rm s} \approx 10\,{\rm km\,s^{-1}}$, then transitions to a quadratic increase in the supersonic regime.

[13] Helium is assumed to be singly ionized, leading to only a small contribution to the drag force. For much hotter stars, such as the central stars of planetary nebulae, helium may be doubly ionized, which leads to a fourfold increase in its Coulomb drag contribution, which is significant for $w < 5\,{\rm km\,s^{-1}}$.

[14] All metals are lumped together as a single species, assuming standard H II region gas-phase abundances. They are dominated by C and O, with minor contributions from N and Ne. The total abundance is 8.5×10^{-4} and the effective atomic weight is 15.3. All are assumed to be doubly ionized. Their largest relative contribution to the drag force is for $w < 2\,{\rm km\,s^{-1}}$, but is less than 1% even there.

[15] To simplify the exposition, the gas pressure in this section is calculated assuming a fully ionized, pure hydrogen plasma, yielding $P_{\rm gas} = 2nkT$. For typical ISM abundances, the contribution of helium and its corresponding electrons yield a correction to this of order 5%. The required modifications when a cool star interacts with a predominantly neutral gas stream are discussed later.

As $|\phi|$ increases, long-range electrostatic interactions with protons within the Debye radius (Coulomb drag) become increasingly important at subsonic relative velocities, as shown by the solid lines in Figure 5). However, the Coulomb drag has a peak when w is equal to the thermal speed of the colliders, which is $\approx 10\,\mathrm{km\,s^{-1}}$ for protons, giving a maximum strength of

$$f_{\max} = 0.5\,(\ln\Lambda)\,\phi^2 f_* \approx 10\,\phi^2 f_* \,, \tag{38}$$

where Λ is the plasma parameter (number of particles within a Debye volume), such that $\ln\Lambda = 23.267 + 1.5\ln T_4 - 0.5\ln n$. At highly super-thermal speeds, the Coulomb drag falls asymptotically as $f_{\text{drag}} \propto 1/w^2$. The thermal speed of electrons is higher than that of the protons by a factor of $(m_p/m_e)^{1/2}$, so that the electron Coulomb drag (solid light blue line) gives a second peak of similar strength, but at $w \approx 430\,\mathrm{km\,s^{-1}}$. The behavior of f_{drag} in all these different regimes is summarised in Table 2, in terms of ϕ and $w_{10} = w/10\,\mathrm{km\,s^{-1}}$. This is further illustrated in Figure 6, where each of the drag regimes is located on the $(w, |\phi|)$ plane.

2.2.2 *Gas–grain separation: drift and rip*

In Appendix B we calculate the behaviour of an incoming stream of dust grains, subject only to the repulsive radiation force from a star. For an initial inward radial trajectory, the dust grain motion is decelerated and turned around, reaching a minimum radius R_{**}, given by equation (B2). This drag-free radiative turnaround radius, R_{**}, is smaller for higher initial inward velocities, but is independent of the density of the incoming stream. We are now in a position to see how gas–grain drag will modify this picture.

From equations (B1) and (37), we can write the radiation force acting on a grain as

$$f_{\text{rad}} = Q_{\text{p}}\,\Xi\,f_* \,, \tag{39}$$

where Q_{p} is the grain's radiation pressure efficiency (see footnote 22 in Appendix B) and Ξ is the local radiation parameter, defined as the ratio of direct stellar radiation pressure to gas pressure:

$$\Xi \equiv \frac{P_{\text{rad}}}{P_{\text{gas}}} \approx \frac{L}{4\pi R^2 c\,(2nkT)} \,, \tag{40}$$

where the last expression corresponds to the optically thin limit. The grain potential ϕ is also primarily determined by Ξ, as shown in Appendix A and the inset graph of Figure 7, but with a slow dependence, which can be approximated as

$$\phi(\Xi) \approx 1.5\big(2.3 + \ln\Xi\big) \,. \tag{41}$$

There are also slight secondary dependencies on the grain composition and stellar spectrum. The relationship given in eq. (41) is appropriate for graphite grains and for stellar effective temperatures in the range 20 kK to 30 kK. For hotter stars than this, ϕ should be multiplied by a further factor of 1.5, while for silicate grains it should be divided by 1.5.

In the outer regions of the photoionized volume around an OB star, close to the ionization front, the radiation parameter is low, with typical value $\Xi \sim 0.1$. In this regime, the negative charge current at the grain surface due to electron collisions is roughly in balance with the positive current due to the ultraviolet photoelectric effect (Weingartner & Draine 2001), leading to a low grain potential, $|\phi| < 1$, which may be positive or negative. The low Ξ means that the radiative force is also weak: $f_{\text{rad}} \sim 0.1 f_*$ from equation (39) if $Q_{\text{p}} \sim 1$ at UV wavelengths, which is true for all but the smallest grains. Thus, from the equations for f_{drag} given in Table 2, the radiative force can be balanced by Epstein drag if $w_{10} \sim 0.1$, leading to a small equilibrium drift velocity, $w_{\text{drift}} < 1\,\mathrm{km\,s^{-1}}$, of the grains with respect to the gas. This drift is much smaller than the inward stream velocities that we are considering ($v_\infty > 10\,\mathrm{km\,s^{-1}}$), so the dust follows the gas stream at a slightly reduced velocity (< 10%), and (by mass conservation) a slightly increased density. Each grain exerts an exactly opposite force to f_{drag} upon the gas, but since the dust-gas mass ratio, Z_{d}, is small, this produces a negligible acceleration of the gas.

Table 3. Critical values of radiation parameter at the rip point: $\Xi_\dagger$

Spectrum	Grain composition: Graphite	Silicate
B star	1000 ± 400	350 ± 150
O star	3000 ± 500	2500 ± 500

Calculated from the Cloudy models shown in Figure A2. Uncertainties represent variations with grain size and gas density. See Appendix A for further details.

As the dusty stream approaches the star, the radiation parameter Ξ will increase, with a dependence of R^{-2} once the stream is well inside the ionization front. This increases f_{rad} (eq. [39]), but also increases the grain potential, ϕ (eq. [41]) due to the increasing dominance of grain charging by photoelectric ejection. Initially, this results in a lowering of the equilibrium drift velocity to $w_{10} \sim 0.01$ as the Coulomb drag kicks in (see Appendix A). However, at smaller radii the slow logarithmic increase in $\phi(\Xi)$ means that the drift velocity must start increasing again to accommodate the linear increase of $f_{\text{rad}}(\Xi)$. Eventually, f_{rad} exceeds $f_{\max}$, the maximum drag force that proton Coulomb interactions can provide (eq. [38]). This occurs at a critical value of the radiation parameter, which we denote the *rip point*: $\Xi_\dagger \sim 1000$. The variations in $\Xi_\dagger$ with star and grain parameters, which are of order ± 0.5 dex, are listed in Table 3 and illustrated graphically in Figure A2.

2.2.3 *Existence conditions for dust waves*

In order for a separate dust wave to exist, it is necessary for the grains to decouple from the incoming gas stream before the stream hits the hydrodynamic bow shock caused by the stellar wind. The radius of the rip point, $R_\dagger$, can be expressed in terms of R_*, the fiducial optically thick bow shock radius introduced in § 2.1:

$$R_\dagger = \frac{v_\infty}{c_{\text{s}}}\,\Xi_\dagger^{-1/2} R_* \approx v_{10}\,\Xi_\dagger^{-1/2} R_* \,, \tag{42}$$

where we have made use of equations (3) and (40). The wind bow shock radius is $R_0 = \eta^{1/2} R_*$ (eq. [12]), where η is the wind momentum efficiency (eq. [13]). Therefore, the condition $R_\dagger > R_0$ becomes

$$v_{10} > v_{10,\min} = \left(\Xi_\dagger\,\eta\right)^{1/2} . \tag{43}$$

For O stars, the wind efficiency is generally high ($\eta > 0.1$) and $\Xi_\dagger > 2000$ (Tab. 3), so that dust waves can only exist when the stream velocity is very high ($v_\infty > 150\,\mathrm{km\,s^{-1}}$). For B stars, in contrast, the wind can be much weaker ($\eta < 0.01$) and $\Xi_\dagger$ is also smaller, so that dust waves are permitted by this criterion for much lower stream velocities: ($v_\infty > 30\,\mathrm{km\,s^{-1}}$).

However, there are other conditions that need to be satisfied in order for the dust wave to exist. For instance, the drag-free turnaround radius must also be outside the bow shock: $R_{**} > R_0$, otherwise the radiation is incapable of repelling the grain opportunely, even once

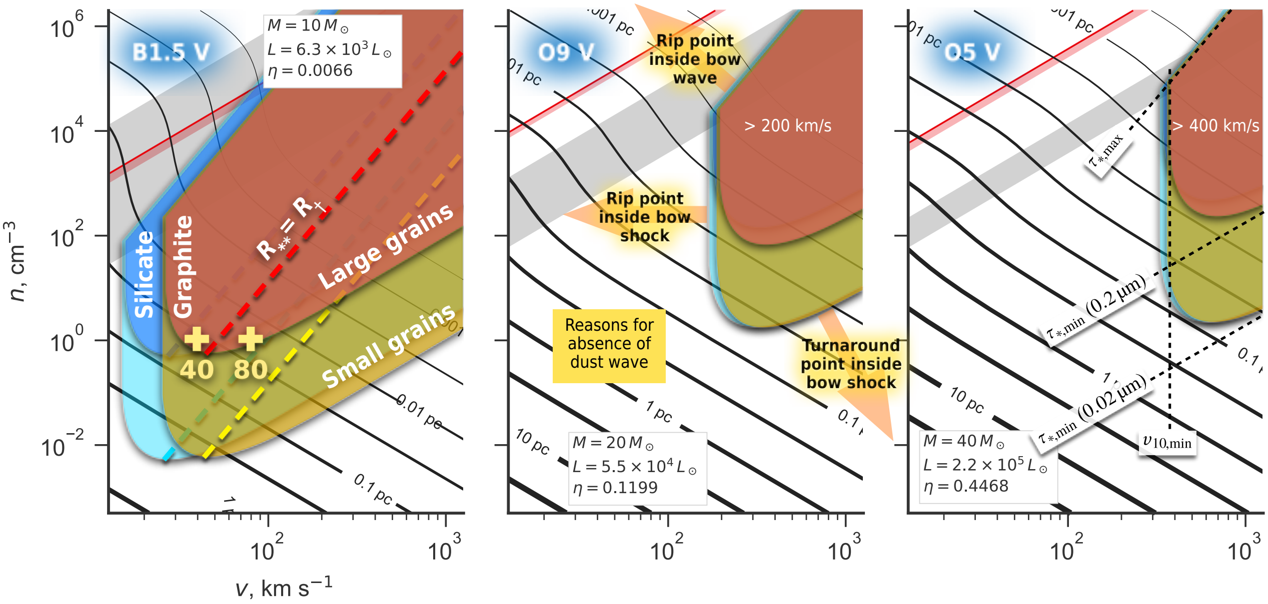

Figure 8. Regions of stream parameter space (v, n) where dust waves may form around main-sequence OB stars of $10\,\mathrm{M}_\odot$, $20\,\mathrm{M}_\odot$ and $40\,\mathrm{M}_\odot$ (see Tab. 1). Figure is similar to Fig. 2, except that the velocity axis is logarithmic and extends out to $1000\,\mathrm{km\,s^{-1}}$. Overlapping colored shapes show parameters where dust waves may be allowed in the cases of large ($a = 0.2\,\mu\mathrm{m}$) and small ($a = 0.02\,\mu\mathrm{m}$) graphite and silicate grains, as labeled in the left panel. For (v, n) outside of these shapes, dust waves cannot occur for the reasons indicated by labeled orange arrows in the center panel. Labeled dashed lines in the right panel show the correspondence between the region boundaries and each dust wave existence condition given in equations (43, 45, 46). Heavy dashed lines in the left panel show where the rip point and the drag-free turnaround radius coincide. Dust waves above these lines are drag confined, while dust waves below the lines are inertia confined.

it has decoupled from the gas. From equations (3), (9), and (B2) we find

$$\frac{R_{**}}{R_*} = \frac{2\sigma_\mathrm{d} Q_\mathrm{p} \tau_*}{\kappa m_\mathrm{d}} \,, \tag{44}$$

so, if we define a single-grain opacity as $\kappa_\mathrm{d} = \sigma_\mathrm{d} Q_\mathrm{p}/m_\mathrm{d}$, then this condition becomes

$$\tau_* > \tau_{*,\mathrm{min}} = 0.5\,\frac{\kappa}{\kappa_\mathrm{d}}\,\eta^{1/2} \,. \tag{45}$$

The average value of the factor κ/κ_d over the entire grain population must be equal to the dust–gas mass ratio, $Z_\mathrm{d} \approx 0.01$, but the factor will vary between grains, according to their size and composition.[16] In particular, it will be relatively larger for the largest grains ($a \approx 0.2\,\mu\mathrm{m}$), which dominate the total dust mass, and smaller for the smaller grains ($a \approx 0.02\,\mu\mathrm{m}$), which dominate the UV opacity. Given the dependence of τ_* on the stream parameters (eq. [15]), for a given stellar luminosity this condition corresponds to a minimum value for n/v_∞^2.

A third condition comes from requiring $R_\dagger > R_0$ in the radiation bow wave regime (see § 2.1.1), where $R_0 \approx 2\tau_* R_*$. This yields

$$\tau_* < \tau_{*,\mathrm{max}} = 0.5\, v_{10}\, \Xi_\dagger^{-1/2} \,, \tag{46}$$

which, for a given stellar luminosity, corresponds to a maximum value for n/v_∞^4. Thus, for a given stream velocity that satisfies equation (43), equations (45, 46) determine respectively the minimum and maximum stream density for which a dust wave can exist.

The combined effects of the three conditions are illustrated in Figure 8 for each of the three example main sequence stars from Table 1. Further restrictions on the existence of dust waves arise when the effects of magnetic fields are considered, as will be discussed in § 2.2.6 below.

2.2.4 Grain trajectories along the symmetry axis

What happens to the dust grain following this catastrophic breakdown of gas–grain coupling depends on the relation between the rip point radius, $R_\dagger$, and the drag-free radiative turnaround radius, R_{**}. If $R_\dagger > R_{**}$, then the grain's inertia will still carry it in as far as R_{**} and the initial trajectory will be almost identical to that described in Appendix B for the drag-free case. However, after being turned around by the radiation field and pushed out past $R_\dagger$ again, the grain will *recouple* to the gas and be dragged back for a second approach.[17] We will refer to this as an *inertia-confined dust wave*. From equations (42, 44, 46), the condition $R_\dagger > R_{**}$ corresponds to $\tau_* < (\kappa/\kappa_\mathrm{d})\tau_{*,\mathrm{max}}$, which is indicated by dashed lines in the left panel of Figure 8. If, on the other hand, $R_\dagger < R_{**}$, then the tail wind provided by the gas carries the grain closer to the star than its inertia would naturally take it. When the grain finally decouples at $R_\dagger$ it experiences a much higher unbalanced f_rad, which can initially accelerate it to outward velocities significantly higher than the inflow velocity if $R_\dagger \ll R_{**}$. We will refer to this case as a *drag-confined dust wave*.

[16] Remember that κ is the opacity per unit mass of gas, while κ_d is the opacity per unit mass of a particular grain. In both cases, averaged over the stellar spectrum.

[17] If the initial impact parameter of the trajectory is not strictly $b = 0$, then the resultant lateral component of f_rad will mean that b will be much increased for the second approach.

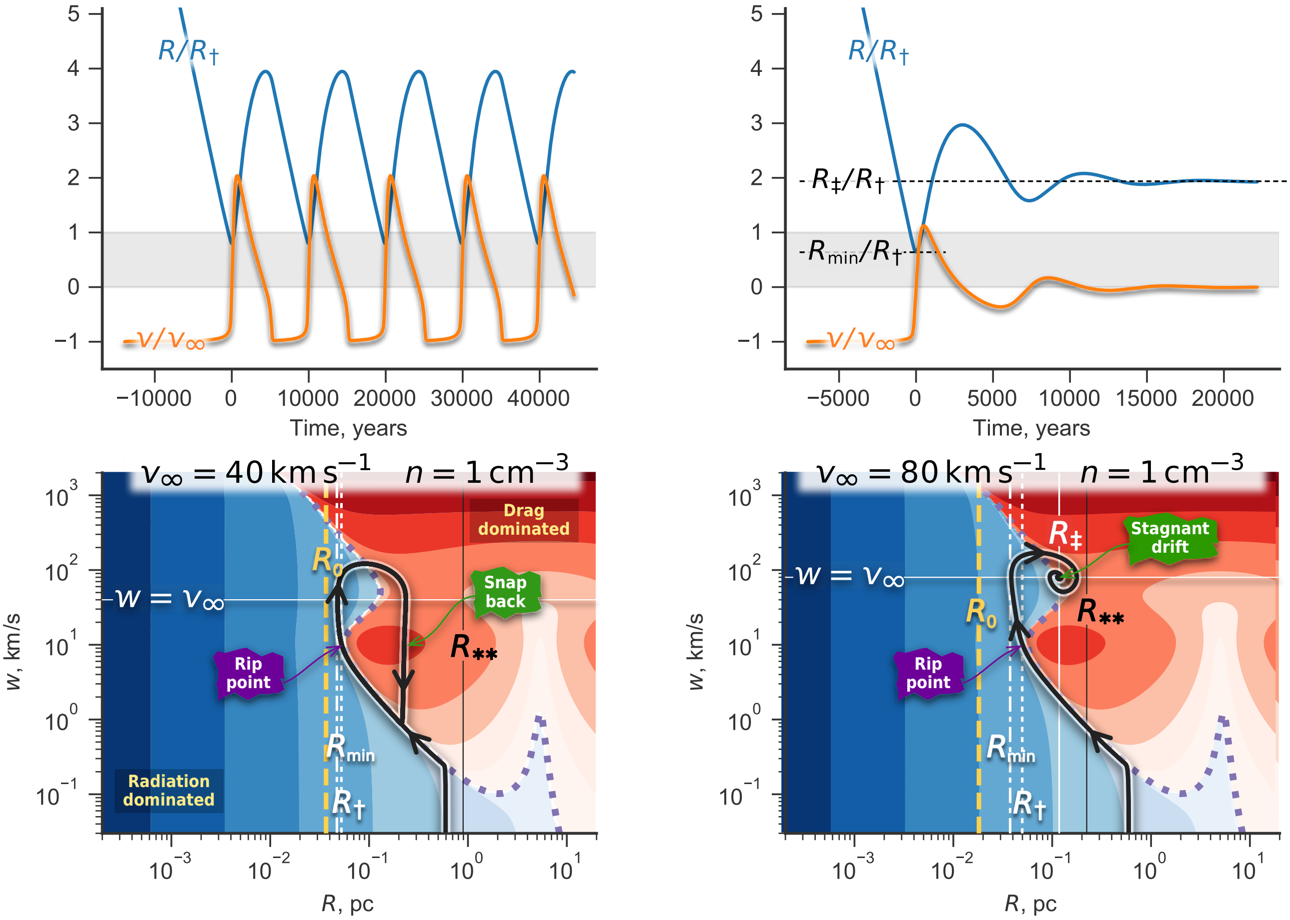

Figure 9. Trajectories of small graphite grains ($a = 0.02\,\mu$m) at impact parameter $b = 0$ for two example cases (see yellow "+" symbols in left panel of Fig. 8), which differ only in the stream velocity: $v = 40\,\mathrm{km\,s^{-1}}$ (left panels) and $80\,\mathrm{km\,s^{-1}}$ (right panels). In both cases, the stream density is $n = 1\,\mathrm{cm^{-3}}$ and the central star is a $10\,\mathrm{M_\odot}$ main-sequence B star (see Tab. 1). Upper panels show the evolution of grain radius, R (blue curve, normalized by the rip point radius, $R_\dagger$), and grain velocity, v (orange curve, normalized by the gas stream velocity). The origin of the time axis is set to the moment of closest approach of the grain to the star: $R = R_{\mathrm{min}}$. Lower panels show the trajectories in phase space: position versus gas–grain relative slip velocity ($w = |v - v_\infty|$). Filled contours show the net force on the grain: $f_{\mathrm{rad}} - f_{\mathrm{drag}}$, with positive values in blue and negative values in red. The heavy dotted line shows where there is no net force: $f_{\mathrm{rad}} = f_{\mathrm{drag}}$. The grain trajectory (thick, solid black line with arrows) initially follows this line, but departs from it after the rip point. In the left panel, the grain enters a limit cycle between decoupling (rip) and re-coupling (snap back). In the right panel, the grain spirals in on the stagnant drift point. See text for further details.

The post-decoupling behavior of the grain depends on the sign of df_{drag}/dw when $w = |v_\infty|$. If this derivative is positive, as is the case in drag regimes II and V (see Tab. 2 and Fig. 6), then the grain can reach a stable equilibrium drift at rest with respect to the star[18] at a point $R_\ddagger$, which we call the *stagnant drift radius*. If the stream velocity is not excessively high ($v_\infty < 150\,\mathrm{km\,s^{-1}}$ when $\phi = 4$, or $< 300\,\mathrm{km\,s^{-1}}$ when $\phi = 16$), then the equilibrium f_{rad} is less than the value at the rip point, requiring a lower value of the radiation parameter: $\Xi_\ddagger < \Xi_\dagger$. The resultant stagnant drift radius is therefore outside the rip point: $R_\ddagger > R_\dagger$.

On the other hand, if $df_{\mathrm{drag}}/dw < 0$ when $w = |v_\infty|$, then the equilibrium is unstable and no stagnant drift is possible. This occurs for drag regime IV, which applies when $\phi > 1$ and $10\,\mathrm{km\,s^{-1}} < v_\infty < 50\,\mathrm{km\,s^{-1}}$. There is also a second unstable regime (partially visible in the upper-right corner of Fig. 6), which is related to the thermal peak in the electron Coulomb drag when $\phi > 30$ and $400\,\mathrm{km\,s^{-1}} < v_\infty < 2000\,\mathrm{km\,s^{-1}}$, but this is not relevant to bow shocks around OB stars.[19]

An example of each of these two behaviors is illustrated in Figure 9. The left panels show the case where $v_\infty = 40\,\mathrm{km\,s^{-1}}$, which is in the unstable regime, resulting in periodic "limit-cycle" behavior (the parameters of this model correspond to the yellow "plus" symbol labeled "40" in the left panel of Fig. 8). During the grain's first approach, it starts to follow a phase trajectory (lower left panel) along the $f_{\mathrm{rad}} - f_{\mathrm{drag}} = 0$ contour, corresponding to

[18] Again, this is only strictly true when the impact parameter is zero. However, as we show below, it is a reasonable approximation over a range of impact parameters in the case where the angle between the magnetic field direction and the stream velocity is not too large.

[19] It may apply in other contexts, such as outflows from AGN, since detailed modeling of grain charging around quasars (Weingartner et al. 2006) implies that grain potentials as high as $\phi \sim 100$ can be achieved.

equilibrium drift, in which the grain begins to move a few $\mathrm{km\,s^{-1}}$ slower than the gas stream. Then, when it reaches the rip point ($R = R_\dagger$, $w \approx 10\,\mathrm{km\,s^{-1}}$) it suddenly experiences a large unbalanced outward radiation force (blue region of phase space in Fig. 9). The grain's inward momentum carries it to the point $R_{\min} \approx 0.85 R_\dagger$, before it is expelled at roughly twice the inflow speed. However, after moving outward, it finds itself in a drag-dominated region of phase space (red in the figure), and so recouples to the inflowing gas stream. The recoupling initiates gradually, as the grain's outward motion is slowed and it begins to move inward again, but is completed suddenly once w again falls below $10\,\mathrm{km\,s^{-1}}$, in what we term *snap back*. The net result is that the grain has returned to exactly the same phase track that it started in on, and so repeats the cycle indefinitely.

The right panels of Figure 9 show the case where the stream velocity is doubled to $v_\infty = 80\,\mathrm{km\,s^{-1}}$, but all other parameters remain the same. At this velocity, the equilibrium drift is stable and so the grain can achieve a stagnant drift solution, where it is stationary with respect to the star. The trajectory during the first approach is similar to the previous case, except that the overshoot of the rip point is greater, so that $R_{\min} \approx 0.65 R_\dagger$ in this case. This is a consequence of the fact that the rip point is closer to the drag-free turnaround radius ($R_\dagger / R_{**}$ is larger than in the lower velocity case), so that the grain inertia is relatively more important. A second consequence of this is that the speed of the initial expulsion is not so large, being only a little higher than the inflow velocity. The qualitative difference between the two cases emerges after the first recoupling: instead of the snap back and endless limit cycle, the grain oscillates about the stagnant drift radius with ever decreasing amplitude, so that after a few oscillation periods it has come to almost a complete rest.

2.2.5 *Back reaction on the gas flow*

So far we have ignored the effect of the drag force on the gas stream itself, but it is clear that this must become important as τ_* approaches $\tau_{*,\max}$, since that is the point where the dust wave transitions to a bow wave, in which the dust and gas are perfectly coupled. A full treatment of this problem would require solving the hydrodynamic equations simultaneously with the equations of motion of the dust grains, which is beyond the scope of this paper. Instead, we outline a heuristic approach that qualitatively captures the physics involved.

The maximum drag force experienced by a grain is at the rip point. Since the grain follows a zero-net-force phase track up until that point, this can be written with the help of equations (B1, B2) as

$$f_{\mathrm{drag}}(R_\dagger) = f_{\mathrm{rad}}(R_\dagger) = \frac{m_{\mathrm{d}} v_\infty^2 R_{**}}{2 R_\dagger^2} \tag{47}$$

The timescale of the flow can be characterized by the crossing time $R_\dagger / v_\infty$, but the residence time of the grain at the bow apex will be several times larger than this (see previous section). On the other hand, the average drag force during this residence will be several times smaller than $f_{\mathrm{drag}}(R_\dagger)$ if $R_\ddagger > R_\dagger$, which is typically the case. We therefore parameterize our ignorance via a dimensionless factor, α, which we expect to be of order unity, and write the total impulse imparted to the grain by drag as

$$J_{\mathrm{drag}} \equiv \int f_{\mathrm{drag}}\, dt \approx \alpha f_{\mathrm{drag}}(R_\dagger) \frac{R_\dagger}{v_\infty} = \tfrac{1}{2} \alpha\, m_{\mathrm{d}} v_\infty \frac{R_{**}}{R_\dagger} . \tag{48}$$

By Newton's Third Law, an equal and opposite impulse is imparted to the gas, which will act to decelerate the gas stream as it decouples from the grains. Realistically, J_{drag} should be summed

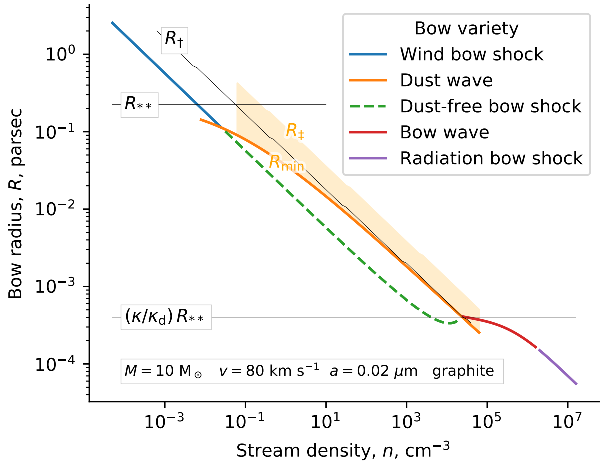

Figure 10. Bow radius as a function of stream density for a stream of initial velocity $80\,\mathrm{km\,s^{-1}}$, which interacts with a $10\,\mathrm{M_\odot}$ main-sequence B star. This corresponds to a vertical slice through the left panel of Fig. 8. At low densities, the hydrodynamic bow shock (blue line) is larger than the drag-free turnaround radius for small carbon grains, meaning that a grain's inertia carries it into the bow shock along with the gas, even though the gas–grain coupling is not particularly strong. At densities above about $0.05\,\mathrm{cm^{-3}}$, however, this is no longer true and a separate dust wave forms outside of the hydrodynamic bow shock, which is now dust-free (green dashed line). The grains in the dust wave will occupy a range of radii (pale orange shading) between $R_{\min}$ (solid orange line) and $R_\ddagger$, the stagnant drift radius. At densities above about $1000\,\mathrm{cm^{-3}}$, the gas stream starts to feel the effect of passing through the dust wave, and above $3 \times 10^4\,\mathrm{cm^{-3}}$, the dust wave and bow shock merge to form a radiative bow wave (red line), which becomes an optically thick radiative bow shock (purple line) above $10^6\,\mathrm{cm^{-3}}$.

over the grain size distribution, but for simplicity we assume that all grains are identical, so that the mass of gas that accompanies each grain is given by

$$m_{\mathrm{gas}} = \frac{m_{\mathrm{d}}}{Z_{\mathrm{d}}} = m_{\mathrm{d}} \frac{\kappa_{\mathrm{d}}}{\kappa} . \tag{49}$$

If the gas remains supersonic after decoupling, then thermal pressure can be ignored and the gas will suffer a change in momentum equal to J_{drag}, so that its velocity is reduced by $\Delta v = J_{\mathrm{drag}} / m_{\mathrm{gas}}$, which by equations (42, 44, 46, 48, 49) is

$$\Delta v = \tfrac{1}{2} \alpha \frac{\tau_*}{\tau_{*,\max}} . \tag{50}$$

This deceleration reduces the gas stream's ram pressure before it interacts with the central star's stellar wind. The radius of the dust-free bow shock formed by this interaction is therefore increased by a factor $(1 - \Delta v / v_\infty)^{-1}$ with respect to the case calculated in § 2.1.1, yielding

$$R_{\mathrm{dfbs}} \approx \frac{\eta^{1/2} R_*}{1 - \frac{1}{2} \alpha \tau_* / \tau_{*,\max}} . \tag{51}$$

An example is illustrated in Figure 10, where the dust-free bow shock radius is shown by the green dashed line as a function of stream density, n. This is calculated for fixed stream velocity and grain and star properties, so that $\tau_* \propto n^{1/2}$ (eq. [15]). In order for R_{dfbs} to match the dust-wave and bow-wave radii at the point where they cross at $\tau_* = \tau_{*,\max}$, we find $\alpha \approx 1.5$ is required. It can be seen that the gas deceleration is negligible over most of the density range for which a separate dust wave arises. Only for $n > 10^3\ \mathrm{cm^{-3}}$ does R_{dfbs} begin to curve up from the general $n^{-1/2}$ trend, becoming essentially flat at a value $R_{\mathrm{dfbs}} \approx (\kappa/\kappa_{\mathrm{d}})R_{**}$ until full-coupling is established at $n > 3 \times 10^4\ \mathrm{cm^{-3}}$. Note, however, that the treatment described here is very approximate: it does not take into account the shock that will form once J_{drag} reaches an appreciable fraction of $m_{\mathrm{gas}} v_\infty$ and, additionally, it includes a factor, α, whose value has not been rigorously justified. More detailed modeling is required to fully understand the bow behavior in this transition regime.

2.2.6 *Magnetic effects on grain trajectories*

An important effect that we have not considered up to now is the Lorentz force on charged grains due to the plasma's magnetic field:

$$\boldsymbol{f}_{\mathrm{B}} = \frac{z_{\mathrm{d}} e}{c}\, \boldsymbol{w} \times \boldsymbol{B}\ . \tag{52}$$

The direction of the force is perpendicular both to the magnetic field, $\boldsymbol{B}$, and to the relative velocity, $\boldsymbol{w}$, of the grain with respect to the plasma. If $\boldsymbol{w}$ and $\boldsymbol{B}$ (as seen by the grain) are changing slowly, compared with the gyrofrequency, $\omega_{\mathrm{B}} = z_{\mathrm{d}} e B / m_{\mathrm{d}} c$, then the grain motion perpendicular to $\boldsymbol{B}$ is constrained to be a circle of radius equal to the Larmor radius:

$$r_{\mathrm{B}} = \frac{m_{\mathrm{d}} c w_\perp}{|z_{\mathrm{d}}| e B}\ , \tag{53}$$

where $B = |\boldsymbol{B}|$ and $w_\perp$ is the perpendicular component of $\boldsymbol{w}$. The component of $\boldsymbol{w}$ parallel to $\boldsymbol{B}$ is unaffected by $\boldsymbol{f}_{\mathrm{B}}$, so the resultant trajectory is helical.

The relative importance of the magnetic field can be characterized by the ratio of the Larmor radius to the minimum radius, R_{min}, reached by the grain in the dust wave (see § 2.2.4), where $R_{\mathrm{min}} \approx R_\dagger$ for drag-confined dust waves, or $R_{\mathrm{min}} \approx R_{**}$ for inertia-confined dust waves. We write the field strength in terms of the Alfvén speed,

$$v_{\mathrm{A}} = \frac{B}{(4\pi \rho_{\mathrm{gas}})^{1/2}} = 1.9\, \frac{B}{\mu\mathrm{G}} n^{-1/2}\ \mathrm{km\,s^{-1}}\ , \tag{54}$$

and the grain charge $z_{\mathrm{d}} e$ in terms of the potential ϕ (eq. [36]) to obtain

$$\frac{r_{\mathrm{B}}}{R_\dagger} = 0.0140\, a_{\mu\mathrm{m}}^2\, \frac{w_\perp}{v_{\mathrm{A}}} \left(\frac{\Xi_\dagger}{L_4 T_4}\right)^{1/2} \frac{\rho_{\mathrm{d}}}{\phi_\dagger} \tag{55}$$

and

$$\frac{r_{\mathrm{B}}}{R_{**}} = 0.0544\, a_{\mu\mathrm{m}}^3\, \frac{w_\perp}{v_{\mathrm{A}}}\, \frac{v_{10}^2}{n^{1/2}}\, \frac{1}{L_4 T_4}\, \frac{\rho_{\mathrm{d}}^2}{Q_{\mathrm{P}} \phi_{**}}\ , \tag{56}$$

where $a_{\mu\mathrm{m}} = a / 1\ \mu\mathrm{m}$, ρ_{d} is the grain material density in $\mathrm{g\,cm^{-3}}$, and we have made use of equations (14, 42, B2).

If $r_{\mathrm{B}}/R_{\mathrm{min}} \ll 1$, then the grains are so strongly coupled to the field that they can be treated in the guiding-center approximation, in which the trajectory is decomposed into a tight circular gyromotion around the field lines, plus a sliding of the guiding center along the field lines, which is governed by the radiation and drag forces (we ignore the slow $\boldsymbol{f} \times \boldsymbol{B}$ drift across the field lines). In the opposite limit, $r_{\mathrm{B}}/R_{\mathrm{min}} \gg 1$, magnetic coupling is so weak that the results of the previous sections are scarcely modified. Assuming $w_\perp \sim v_\infty$ and adopting a threshold of $r_{\mathrm{B}}/R_{\mathrm{min}} < 0.1$, equations (55, 56) can be transformed into conditions on the stream velocity (in $\mathrm{km\,s^{-1}}$) where tight magnetic coupling will apply:

$$v_\infty < v_{\mathrm{tight}} \approx \begin{cases} \text{drag-confined:} & 0.8\, a_{\mu\mathrm{m}}^{-2}\, v_{\mathrm{A}}\, L_4^{1/2} \\ \text{inertia-confined:} & 6\, a_{\mu\mathrm{m}}^{-1}\, v_{\mathrm{A}}^{1/3}\, n^{1/6}\, L_4^{1/3} \end{cases}\ , \tag{57}$$

where we have substituted typical values of the minor parameters $\Xi_\dagger$, $\phi_\dagger$, ϕ_{**}, ρ_{d}, T_4.[20] It is apparent that v_{tight} is very sensitive to the grain size. For instance, taking a typical H II region value of $v_{\mathrm{A}} = 2\ \mathrm{km\,s^{-1}}$ (Arthur et al. 2011) and $L_4 = 0.63$ (Tab. 1, B1.5 V star), then for the drag-confined case $v_{\mathrm{tight}} \approx 30\ \mathrm{km\,s^{-1}}$ for $0.2\ \mu\mathrm{m}$ grains but $v_{\mathrm{tight}} \approx 3000\ \mathrm{km\,s^{-1}}$ for $0.02\ \mu\mathrm{m}$ grains. Thus, for typical stream velocities of $20\ \mathrm{km\,s^{-1}}$ to $100\ \mathrm{km\,s^{-1}}$, the small grains are always tightly coupled to the magnetic field, but the large grains are only loosely coupled for the faster streams.

We now investigate how the results of the previous sections are modified by magnetic fields in the tight coupling limit. For simplicity, we assume a uniform field in the incoming stream, with field lines oriented at an angle θ_{B} to the velocity vector that defines the bow axis. We also assume a super-alfvénic stream, $v_\infty > v_{\mathrm{A}}$, so that the radius, R_0, of the wind bow shock is unaffected, and take $t_* \ll \tau_{*,\mathrm{max}}$, so that the back-reaction of the grain drag on the plasma is negligible (see previous section) and B remains uniform in magnitude and direction in the dust wave region, outside of the bow shock. In Appendix B3, we derive results in the limit of zero gas–grain drag, which is appropriate for inertia-confined dust waves.

3 CASE STUDIES

Carina mid-infrared bow shocks (Sexton et al. 2015) are in a high density environment, $1000\ \mathrm{cm^{-3}}$, so they may be bow waves. There seems to be spectral types for most of them: B0 (but supergiant) to O7. Sizes are 3 to 12 arcsec, which at Carina (2.3 kpc) is 0.033 pc to 0.134 pc.

Amazingly, the size/density combination gives regions that overlap with the dust wave region for both the $20\ \mathrm{M_\odot}$ and $40\ \mathrm{M_\odot}$ case. And implying velocities of $30\ \mathrm{km\,s^{-1}}$ to $50\ \mathrm{km\,s^{-1}}$. This is more believable than the $10\ \mathrm{km\,s^{-1}}$ that they quote, since that would not give a shock at all. This would imply $\tau > \eta \approx 0.1$, so the bow luminosity should be 10% of the star luminosity, so getting on for $10^4\ \mathrm{L_\odot}$.

Two small bows in M42:

θ^1 Ori D (Ney–Allen nebula) (Robberto et al. 2005)

LP Ori: B1.5V star, like our $10\ \mathrm{M_\odot}$ example. Radius about $3''$, so 0.005 pc. With $v = 80$ that would clearly be a dust wave and would require $100\ \mathrm{cm^{-3}}$ to $1000\ \mathrm{cm^{-3}}$. Gaia distance (408 ± 11) pc

Ones that Ochsendorf claims are dust waves (Narrator: they aren't).

4 SUMMARY AND DISCUSSION

How different regions of the Π–Λ plane are populated. Bottom-right quadrant hard to get to (except for standing wave oscillations), but may be due to finite shell thickness, which (for low Mach number) will be more apparent in the wings, which might decrease Λ more than Π. Fact that thin-shell solutions should trace the contact discontinuity, but in some cases it may be only the inner or the outer shell that is visible.

Justification for standing waves: Fig. 3 of Meyer et al. (2016) shows a time sequence of thin-shell instability, which looks a bit like a standing wave. But much larger amplitude than we are considering.

Deviations from axisymmetry as an alternative to oscillations.

[20] The most significant systematic variation in v_{tight} from these suppressed parameters is due to grain composition, yielding slightly higher values for graphite than for silicate (± 0.15 dex).

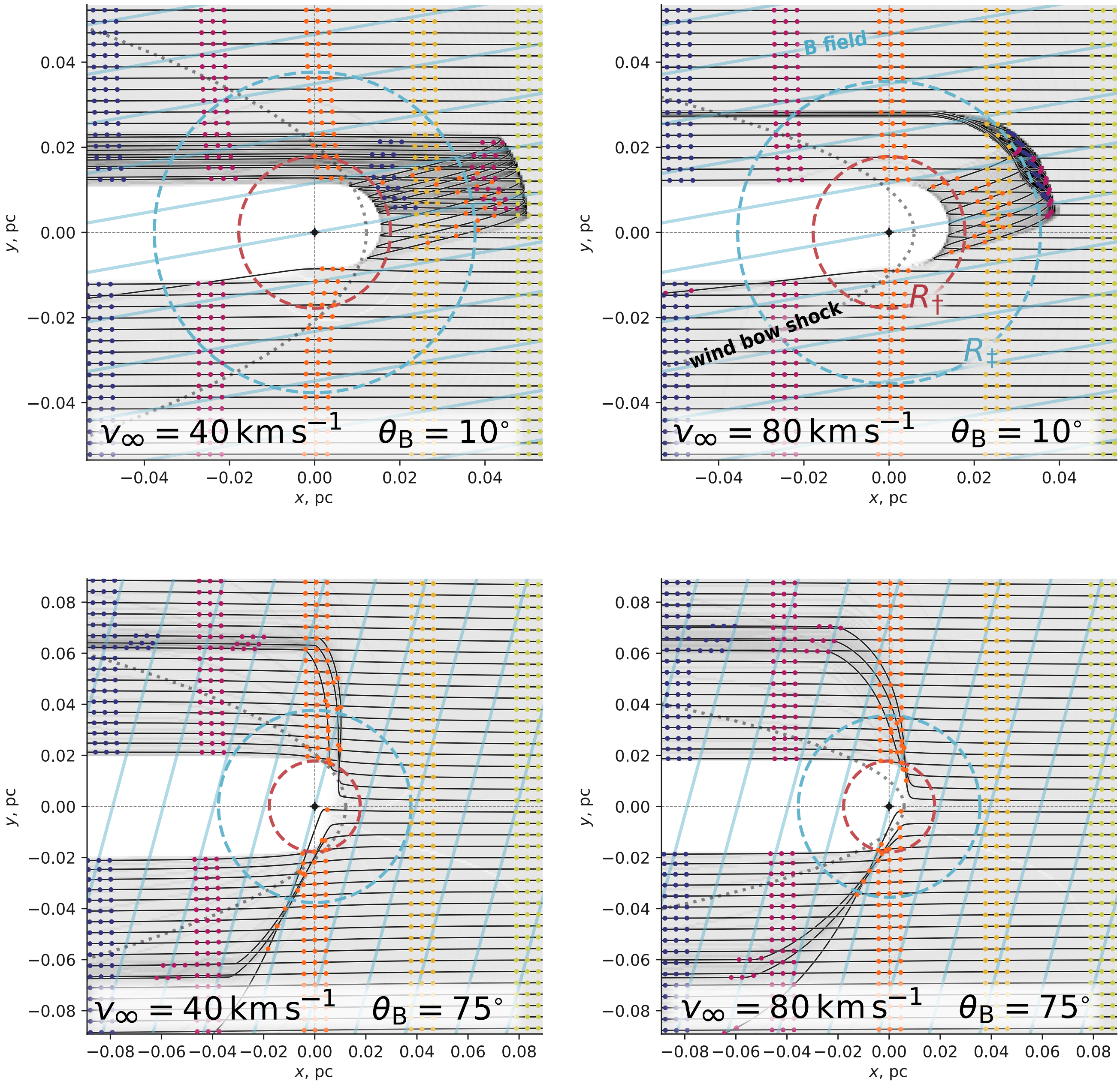

Figure 11. Drag-confined dust waves with tight magnetic coupling. Upper panels show a quasi-parallel field, $\theta_\mathrm{B} = 10^\circ$, while lower panels show a quasi-perpendicular field, $B = 75^\circ$. Left panels show an incident stream velocity of $v_\infty = 40\,\mathrm{km\,s^{-1}}$, while right panels show $v_\infty = 80\,\mathrm{km\,s^{-1}}$. In all cases, the stream density is $n = 10\,\mathrm{cm^{-3}}$ and the calculations are performed for small graphite grains, $a = 0.02\,\mu\mathrm{m}$, and the $10\,\mathrm{M_\odot}$ main-sequence B star. Continuous black lines show grain trajectories, with triplets of colored symbols indicating the progress of individual cohorts, which entered from the right edge at a particular time. Continuous blue lines show the magnetic field, which flows from right to left along with the incident stream. The radius of the rip point, $R_\dagger$, and the stagnant drift point, $R_\ddagger$, are shown respectively by red and blue dashed lines. The approximate shape of the wind-supported bow shock is shown by the dotted gray line. The calculations are no longer valid after trajectories cross this surface.

4.1 The case of inside-out bows

So far, we have considered the case where the inner source dominates the radiation, while dust is present only in the outer stream, which applies to hot stars interacting with the ISM. However, in the case of cool stars, the inner wind will also be dusty. Examples are the red supergiant (RSG) phase of high-mass evolution, or the asymptotic giant branch (AGB) stage of low/intermediate-mass evolution. In both these cases, it is still the inner source that provides the radiation field. However, not all winds are radiatively driven and in those cases it is conceivable that it is the outer source that dominates the radiation field. An example is the case of photoevaporating protoplanetary disks (proplyds) in the Orion Nebula and other H II regions (O'Dell & Wen 1994). In the proplyds, the inner wind is a thermally driven photoevaporation flow (Henney & Arthur 1998; Henney & O'Dell 1999), while the outer stream is the stellar wind from an O star (García-Arredondo et al. 2001).

REFERENCES

Arthur S. J., Hoare M. G., 2006, ApJS, 165, 283
Arthur S. J., Henney W. J., Mellema G., de Colle F., Vázquez-Semadeni E., 2011, MNRAS, 414, 1747
Bertoldi F., Draine B. T., 1996, ApJ, 458, 222
Bohren C. F., Huffman D., 1983, Absorption and scattering of light by small particles. Wiley-VCH
Brott I., et al., 2011, A&A, 530, A115
Canto J., Raga A. C., Wilkin F. P., 1996, ApJ, 469, 729
Draine B. T., Salpeter E. E., 1979, ApJ, 231, 77
García-Arredondo F., Henney W. J., Arthur S. J., 2001, ApJ, 561, 830
Gull T. R., Sofia S., 1979, ApJ, 230, 782
Henney W. J., Arthur S. J., 1998, AJ, 116, 322
Henney W. J., O'Dell C. R., 1999, AJ, 118, 2350
Henney W. J., Arthur S. J., Williams R. J. R., Ferland G. J., 2005, ApJ, 621, 328
Hindmarsh A. C., 1983, IMACS Transactions on Scientific Computation, 1, 55
Jones E., Oliphant T., Peterson P., et al., 2001–2018, SciPy: Open source scientific tools for Python, http://www.scipy.org/
Krtička J., 2014, A&A, 564, A70
Lamers H. J. G. L. M., Cassinelli J. P., 1999, Introduction to Stellar Winds. Cambridge, UK: Cambridge University Press
Lamers H. J. G. L. M., Snow T. P., Lindholm D. M., 1995, ApJ, 455, 269
Landau L., Lifshitz E., 1976, Mechanics, 3rd edn. Course of Theoretical Physics S Vol. 1, Butterworth-Heinemann
Mac Low M.-M., van Buren D., Wood D. O. S., Churchwell E., 1991, ApJ, 369, 395
Meyer D. M.-A., Mackey J., Langer N., Gvaramadze V. V., Mignone A., Izzard R. G., Kaper L., 2014, MNRAS, 444, 2754
Meyer D. M.-A., van Marle A.-J., Kuiper R., Kley W., 2016, MNRAS, 459, 1146
Meyer D. M.-A., Mignone A., Kuiper R., Raga A. C., Kley W., 2017, MNRAS, 464, 3229
O'Dell C. R., Wen Z., 1994, ApJ, 436, 194
Ochsendorf B. B., Tielens A. G. G. M., 2015, A&A, 576, A2
Ochsendorf B. B., Cox N. L. J., Krijt S., Salgado F., Berné O., Bernard J. P., Kaper L., Tielens A. G. G. M., 2014a, A&A, 563, A65
Ochsendorf B. B., Verdolini S., Cox N. L. J., Berné O., Kaper L., Tielens A. G. G. M., 2014b, A&A, 566, A75
Oskinova L. M., Todt H., Ignace R., Brown J. C., Cassinelli J. P., Hamann W.-R., 2011, MNRAS, 416, 1456
Osterbrock D. E., Ferland G. J., 2006, Astrophysics of gaseous nebulae and active galactic nuclei, second edn. Sausalito, CA: University Science Books
Prinja R. K., 1989, MNRAS, 241, 721
Puls J., Vink J. S., Najarro F., 2008, A&ARv, 16, 209
Robberto M., et al., 2005, AJ, 129, 1534
Rodríguez-Ramírez J. C., Raga A. C., 2016, MNRAS, 460, 1876
Sexton R. O., Povich M. S., Smith N., Babler B. L., Meade M. R., Rudolph A. L., 2015, MNRAS, 446, 1047
Spitzer L., 1978, Physical processes in the interstellar medium. New York: Wiley-Interscience
Sternberg A., Hoffmann T. L., Pauldrach A. W. A., 2003, ApJ, 599, 1333
Tarango Yong J. A., Henney W. J., 2018, MNRAS, in preparation
Tenorio-Tagle G., 1979, A&A, 71, 59
Vink J. S., de Koter A., Lamers H. J. G. L. M., 1999, A&A, 350, 181
Vink J. S., de Koter A., Lamers H. J. G. L. M., 2000, A&A, 362, 295
Weidenschilling S. J., 1977, MNRAS, 180, 57
Weingartner J. C., Draine B. T., 2001, ApJS, 134, 263
Weingartner J. C., Draine B. T., Barr D. K., 2006, ApJ, 645, 1188
Wilkin F. P., 1996, ApJ, 459, L31
de Jager C., Nieuwenhuijzen H., van der Hucht K. A., 1988, A&AS, 72, 259
van Buren D., McCray R., 1988, ApJ, 329, L93
van Marle A. J., Meliani Z., Keppens R., Decin L., 2011, ApJ, 734, L26

APPENDIX A: CLOUDY MODELS OF DUST CHARGING AROUND OB STARS

APPENDIX B: DUST WAVES IN THE DRAG-FREE LIMIT

A dust grain of geometrical cross-section σ_{d} situated a distance R from a point source of radiation with luminosity L will experience a repulsive, radially directed radiative force (e.g., Spitzer 1978)

$$f_{\mathrm{rad}} = \frac{\sigma_{\mathrm{d}} Q_{\mathrm{p}} L}{4\pi R^2 c} e^{-\tau} \tag{B1}$$

where Q_{p} is the frequency-averaged[21] radiation pressure efficiency[22] of the grain, c is the speed of light, and τ is the frequency-averaged optical depth between the source and the grain. For simplicity, we will consider only the optically thin case, $\tau \to 0$.

If f_{rad} is the only force experienced by the grain, then it will move on a *ballistic* trajectory, determined by its initial speed at large distance, v_∞, and its impact parameter, b. For $b = 0$, the grain radially approaches the source with initial radial velocity $-v_\infty$, which is decelerated to zero at the distance of closest approach, R_{**}, given by energy conservation:

$$R_{**} = \frac{\sigma_{\mathrm{d}} Q_{\mathrm{p}} L}{2\pi c m_{\mathrm{d}} v_\infty^2} , \tag{B2}$$

where m_{d} is the grain mass. The grain then turns round and recedes from the source along the same radius, reaching a velocity of $+v_\infty$ at large distance. Note that R_{**} as given by equation (B2) is the equivalent of equation (6), except for a single grain considered in isolation, rather than a well-coupled dusty plasma.

For $b > 0$, the trajectory, $R_{\mathrm{d}}(\theta; b)$, is found[23] to be hyperbolic, characterized by an eccentricity, $\varepsilon = \left(1 + 4b^2/R_{**}^2\right)^{1/2}$, and polar angle of closest approach, $\theta_{\mathrm{m}} = \cos^{-1} \varepsilon^{-1}$. The trajectory is symmetrical about θ_{m} and can be written as

$$\frac{R_{\mathrm{d}}(\theta; b)}{R_{**}} = \frac{\frac{1}{2}\left(\varepsilon^2 - 1\right)}{\varepsilon \cos(\theta - \theta_{\mathrm{m}}) - 1} , \tag{B3}$$

with a total deflection angle of $180° - 2\theta_{\mathrm{m}}$, which is equal to $90°$ when $b = 0.5 R_{**}$.

B1 Parallel dust stream

If the incoming dust grains initially travel along parallel trajectories with varying b, but the same v_∞, then deflection by the radiative force

[21] Frequency averages of any quantity x should be understood as weighted by the attenuated source spectrum: $\langle x \rangle_\nu = (L\, e^{-\tau})^{-1} \int_0^\infty x(\nu)\, L_\nu\, e^{-\tau_\nu}\, d\nu$.
[22] For absorption efficiency Q_{abs}, scattering efficiency Q_{scat}, and asymmetry parameter (mean scattering cosine) g, we have $Q_{\mathrm{p}} = Q_{\mathrm{abs}} + (1 - g) Q_{\mathrm{scat}}$ (e.g., § 4.5 of Bohren & Huffman 1983).
[23] The problem is formally identical to that of Rutherford scattering, or (modulo a change of sign) planetary orbits. The method of solution (via introduction of a centrifugal potential term and reduction to a 1-dimensional problem) can be found in any classical mechanics text (e.g., Landau & Lifshitz 1976, § 14).

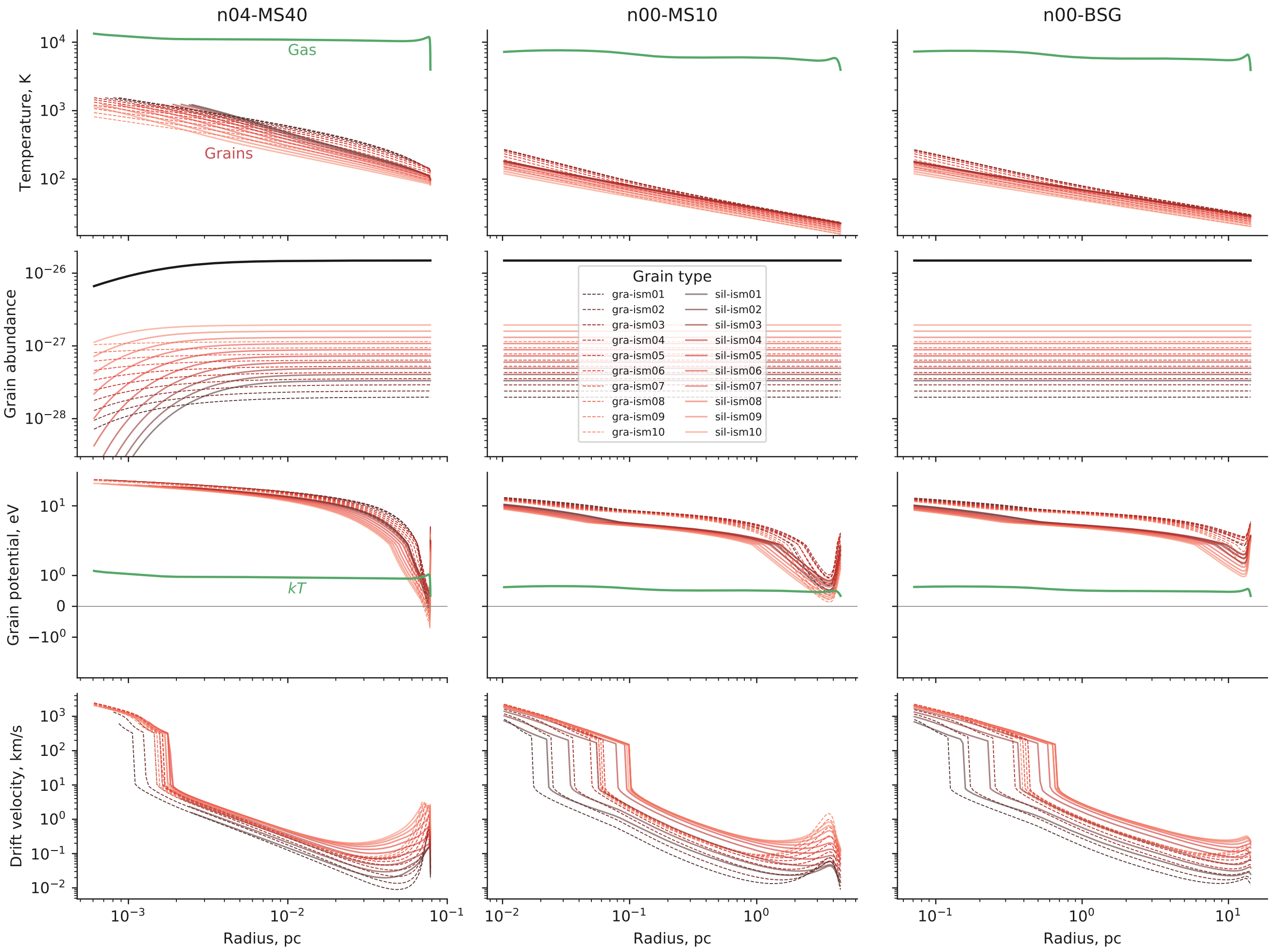

Figure A1. Dust properties as a function of radius from star for three selected Cloudy models. (a) $40\,\mathrm{M}_\odot$ main-sequence star in medium of density $10^4\ \mathrm{cm}^{-2}$. (b) $10\,\mathrm{M}_\odot$ main-sequence star in medium of density $1\ \mathrm{cm}^{-2}$. (c) Blue supergiant star in medium of density $1\ \mathrm{cm}^{-2}$

.

will form a bow-shaped dust wave around the radiation source, as shown in Figure B1. However, the inner edge of the dust wave, $R_{\mathrm{in}}(\theta)$ is not given by the closest approach along individual trajectories, $R_{\mathrm{d}}(\theta_{\mathrm{m}}; b)$, but instead must found by minimizing $R_{\mathrm{d}}(\theta; b)$ over all b for each value of θ, which yields

$$\frac{R_{\mathrm{in}}(\theta)}{R_{**}} = \frac{2}{1+\cos\theta}\,. \tag{B4}$$

This is the polar form of the equation for the confocal parabola, which we have already discussed in detail in Paper I's § 4 and Appendix C. Its planitude and alatude are $\Gamma = \Lambda = 2$ and these are unchanged under projection at any inclination.

B2 Divergent dust stream

If the dust grains are assumed to originate from a second point source, located at a distance D from the radiation source, then the incoming stream will be divergent instead of plane parallel. The individual streamlines are not affected by this change and are still described by equation (B3), except that the trajectory axes for $b > 0$ are no longer aligned with the global symmetry axis, so we must make the substitution $\theta \longrightarrow \theta + \theta_1(b)$, where $\sin\theta_1 = b/D$ (see Fig. 3 of Paper I). We parametrize the degree of divergence as $\mu = R_{**}/D$ and, as before, $R_{\mathrm{d}}(\theta + \theta_1(b, \mu); b)$ is minimized over all trajectories to find the shape of the bow wave's inner edge. This time, the result is a confocal hyperbola:

$$\frac{R_{\mathrm{in}}(\theta;\mu)}{R_{**}} = \frac{1+\varepsilon_\mu}{1+\varepsilon_\mu\cos\theta}\,, \tag{B5}$$

where the eccentricity is (to first order in μ) $\varepsilon_\mu = (1-2\mu)^{-1}$. An example is shown in Figure B1 for $\mu = 0.1$. Unsurprisingly, the resulting bow shape is more open than in the parallel stream case, increasingly so with increasing μ. The planitude and alatude are both equal: $\Pi = \Lambda = 1 + \varepsilon_\mu$.

B3 Tight magnetic coupling

As discussed in § 2.2.6, for small grains ($a < 0.1\,\mu\mathrm{m}$) the Larmor magnetic gyration radius, r_{B} is typically small compared with other length scales of interest, and so the grains are effectively tied to the magnetic field lines. In this approximation, we can calculate the grain dynamics in the drag-free limit using f_{rad} as the sole force as

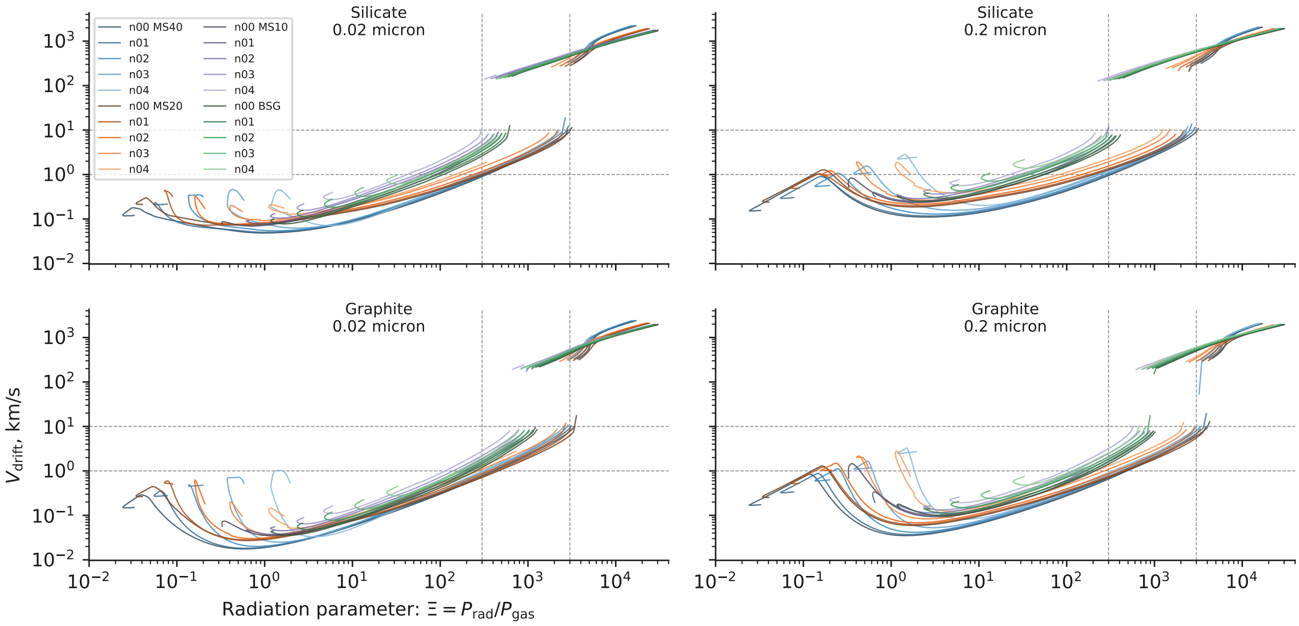

Figure A2. Drift velocity versus radiation parameter Ξ_P. Each line represents a model with ambient density and stellar type as indicated in the key.

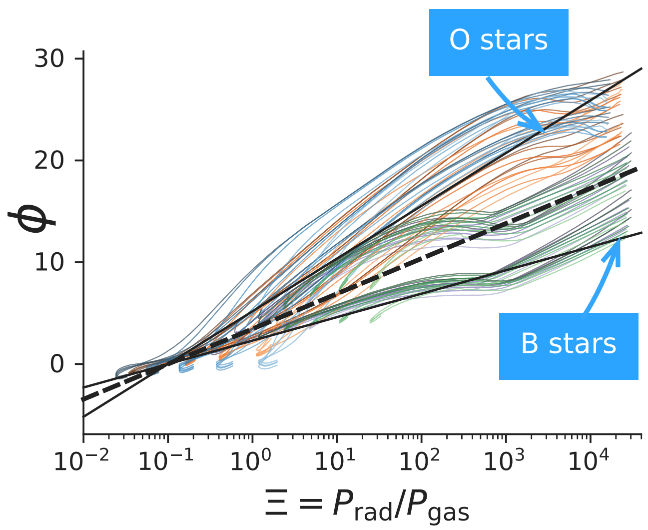

Figure A3. Grain potential versus radiation parameter

above, but this time allowing acceleration only along the field lines. Assuming a uniform magnetic field, the only extra parameter needed is $\theta_{\rm B}$, the angle between the field direction and the direction of the dust stream (assumed to be plane parallel). The radiation force will also produce an out-of-plane drift, given by

$$\boldsymbol{v}_{\rm drift} = \frac{c}{e z_{\rm d}} \frac{\boldsymbol{f}_{\rm rad} \times \boldsymbol{B}}{B^2} \,, \tag{B6}$$

but from equations (53, B1, B2) it follows that

$$\frac{v_{\rm drift}(R_{**})}{v_\infty} = \frac{r_{\rm B}}{2R_{**}} \,, \tag{B7}$$

so it is valid to ignore this drift in the limit of small $r_{\rm B}$.

We now calculate in detail the grain trajectories in this limit for two cases, with the magnetic field oriented parallel and perpendicular to the stream[24] direction, respectively. These are sufficient to give a flavor of the effects of a magnetic field on the dust wave structure. Further models at intermediate angles, and which also include the effects of gas drag, are shown in § 2.2.6.

B3.1 *Parallel magnetic field*

For $\theta_{\rm B} = 0$, the $b = 0$ trajectory is identical to the non-magnetic case since the grain velocity and radiation force are both parallel to the field, which yields zero Lorentz force and zero $\boldsymbol{f} \times \boldsymbol{B}$ drift. Therefore, the axial turnaround radius, R_{**}, is still given by equation (B2), whatever the value of $r_{\rm B}$. For $b > 0$, $f_{\rm rad}$ has a component perpendicular to $\boldsymbol{B}$, which will induce a helical gyromotion around the field lines, but the guiding center must move parallel to the axis if $r_{\rm B} \ll R_{**}$. Thus, the guiding center motion can be found from conservation of potential plus kinetic energy in one dimension:

$$\frac{v^2}{v_\infty^2} + V_{\rm rad} = 1 \,, \tag{B8}$$

where $V_{\rm rad}$ is a suitably normalized potential of the projected radiation force along the field lines (x axis, where $x = R\cos\theta = b\cot\theta$):

$$V_{\rm rad} = R_{**} \int_x^\infty \frac{\cos\theta}{R^2}\, dx = \frac{R_{**}\sin\theta}{b} = \frac{R_{**}}{R} \,. \tag{B9}$$

From equation (B8), the trajectory must turn around when $V_{\rm rad} = 1$, and equation (B9) shows that this occurs at the same spherical radius, $R = R_{**}$, for all impact parameters, b, so that the inner boundary of

[24] In both cases, the stream trajectories are assumed parallel to one another, as in § B1.

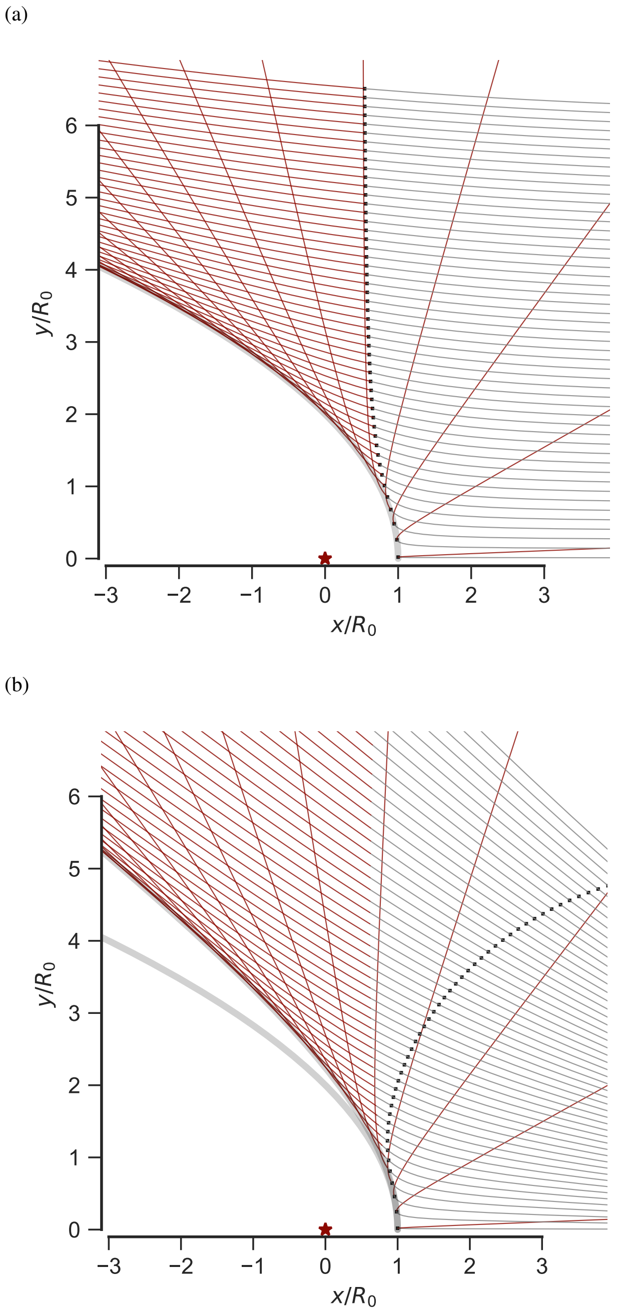

Figure B1. Dust grain trajectories under influence of a repulsive central r^{-2} radiative force. (a) A parallel stream of dust grains approach from the right at a uniform velocity and with a variety of impact parameters (initial y-coordinate). The central source is marked by a red star at the origin, and its radiative force deflects the trajectories into a hyperbolic shape, each of which reaches a minimum radius marked by a small black square. The incoming hyperbolic trajectories are traced in gray and the outgoing trajectories are traced in red. The locus of closest approach of the outgoing trajectories is parabolic in shape (traced by the thick, light gray line) and this constitutes the inner edge of the bow wave. (b) The same but for a divergent stream of dust grains that originates from a source on the x axis at a distance $D = 10R_{**}$ from the origin. In this case, the inner edge of the bow wave is hyperbolic and the parallel stream result is also shown for comparison.

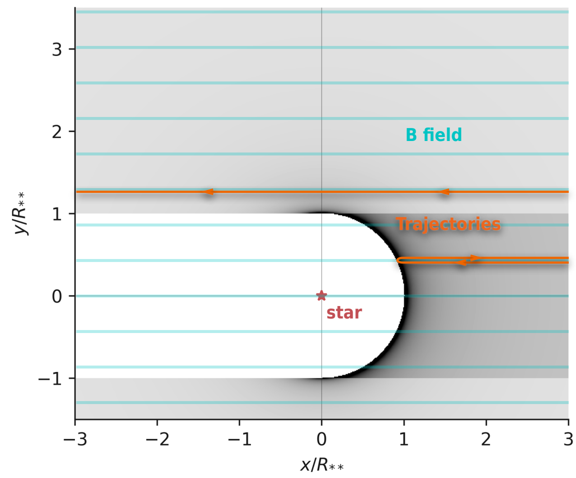

Figure B2. Dust wave formed by action of radiation forces on grains that are tightly coupled to a uniform parallel magnetic field. Two example trajectories, one with $b > R_{**}$ (upper) and one with $b < R_{**}$ (lower) are shown schematically in orange. The orientation of the magnetic field lines is shown in blue. The grayscale image shows the resultant dust density distribution.

the dust wave is hemispherical in shape:

$$\frac{R_{\rm in}(\theta)}{R_{**}} = 1\,, \tag{B10}$$

with $\Pi = \Lambda = 1$. Note, however, that this only applies to streamlines with $b \leqslant R_{**}$. For those with $b > R_{**}$, the maximum $V_{\rm rad}$, which occurs at $x = 0$, is smaller than unity, so that grains on these streamlines slow down as they go past the star, but then speed up again without turning round.

The grain density of the inflowing stream follows from mass continuity as:

$$n_{\rm d}(R) = \frac{n\bar{m}Z_{\rm d}}{m_{\rm d}} \left(1 - R^{-1}\right)^{-1/2}\,, \tag{B11}$$

where for simplicity we assume a single grain species of mass $m_{\rm d}$ and dust-gas ratio $Z_{\rm d}$. The outflowing stream has exactly the same velocity profile as the inflowing one, apart from a change of sign for those streamlines that turn round. Therefore, in the region where the two streams co-exist ($y \leqslant R_{**}$, $x > 0$, and $R > R_{**}$), the total density is double that given by equation (B11). This is illustrated in Figure B2.

B3.2 Perpendicular magnetic field

For $\theta_{\rm B} = 90°$, the guiding center is forced to move at a constant speed in the x direction, so that $x = -v_\infty t$, while the motion in the y direction obeys the ODE:

$$\frac{d^2y}{dx^2} = \tfrac{1}{2} R_{**}\, y \left(x^2 + y^2\right)^{-3/2}\,. \tag{B12}$$

We have been unable to find an analytic solution to this equation, but a numerical solution is shown in Figure B3. When the impact parameter is larger than $b \sim R_{**}$, the trajectories are very similar to in the non-magnetic case (Fig. B1a). As shown in Figure B3b, the interaction of the grain with the radiation field in this large-b regime can be approximated as an impulsive acceleration of magnitude

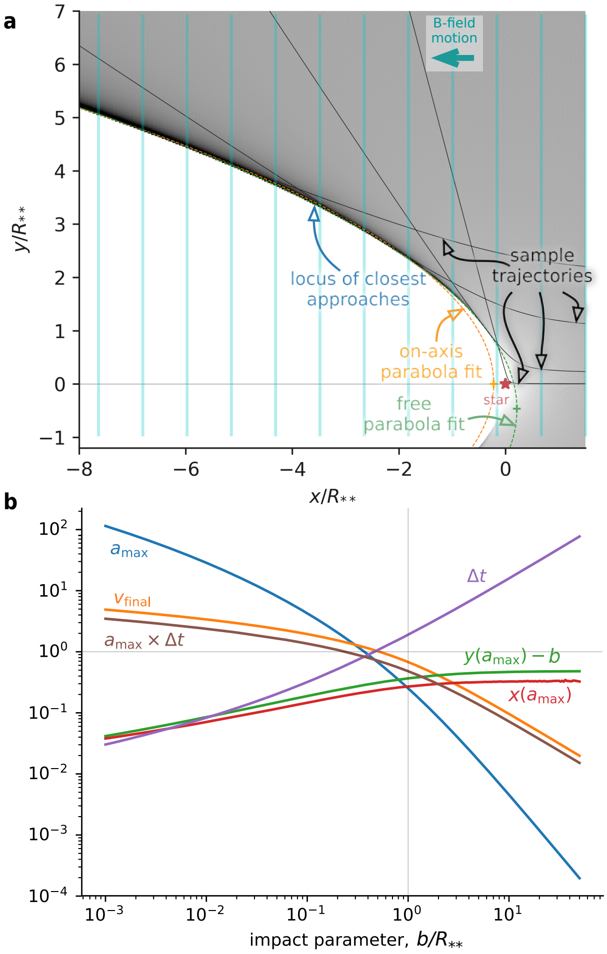

Figure B3. Dust wave formed by action of radiation forces on grains that are tightly coupled to a uniform perpendicular magnetic field. (a) Sample trajectories are shown by thin black lines and the resultant dust density distribution in grayscale. Two parabolic fits to the inner edge of the dust wave in the wing region ($y > R_{**}$) are shown. The orange line shows a simultaneous fit to both wings, while the green line shows a fit to a single wing, in which the parabola apex is not constrained to lie on the axis. The second fit has much smaller residuals, indicating that the overall dust wave shape is "pointier" than a parabola, but this is hard to quantify because the disappearance of the dense shell in the apex region makes it impossible to define R_0 for the bow. (b) Trajectory parameters over a wide range of impact parameters, shown on a log–log scale. Distances are in units of R_{**}, times in units of R_{**}/v_∞, velocities in units of v_∞, and accelerations in units of v_∞^2/R_{**}. The grain's acceleration along the y axis has a maximum value, $a_{\max}$, which occurs at a position $x(a_{\max})$, $y(a_{\max})$, just before the grain is swept past the star, with a duration (FWHM) of Δt. The grain's asymptotic y velocity is v_{final} and the fact that this closely tracks $a_{\max} \times \Delta t$ indicates that the majority of the acceleration occurs in a sharp impulse. The curves tend to straight lines at the right side of the graph, which gives the asymptotic scaling relations discussed in the text.

$\sim b^{-2}$ and duration $\sim b$, producing a final y velocity of $\sim b^{-1}$. Since the x velocity is constant, the total deflection angle is also of order $\sim b^{-1}$. The overlap of the outgoing trajectories produces a dense concentration of grains at the inner edge, which is roughly parabolic in shape. However, for $b < R_{**}$ the remorseless advance of the magnetic field does not allow the grains to slow down and turn round, as they do in the non-magnetic and parallel-field cases. As a result, no dense shell forms in the apex region, but instead there is a diffuse minimum in the density of grains around the star due to the high grain velocities reached there. This means that the apparent morphology of a pure dust wave becomes very sensitive to the radial dependence of the grain emissivity. If this is sufficiently steep, then the apex would coincide with the position of the star, although in practice the presence of a wind-supported bow shock, however small, will complicate the picture.

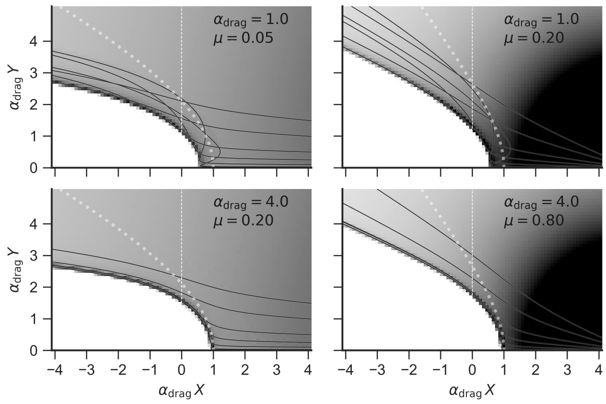

Figure C1. Divergent dragoids

APPENDIX C: EQUATIONS OF MOTION FOR GRAINS WITH RADIATION AND GAS DRAG

To find the dust grain trajectories $R_{\mathrm{d}}(\theta)$ in the presence of radiation and drag forces (§ **??**), we numerically integrate the equations of motion. We define dimensionless cylindrical polar coordinates,

$$(X, Y) = \left(\frac{R_{\mathrm{d}}(\theta)\cos\theta}{R_0}, \frac{R_{\mathrm{d}}(\theta)\sin\theta}{R_0} \right), \tag{C1}$$

and dust grain velocities,

$$(U, V) = \left(\frac{\boldsymbol{v}_{\mathrm{d}} \cdot \hat{\boldsymbol{x}}}{v_\infty}, \frac{\boldsymbol{v}_{\mathrm{d}} \cdot \hat{\boldsymbol{y}}}{v_\infty} \right), \tag{C2}$$

where $\hat{\boldsymbol{x}}$ and $\hat{\boldsymbol{y}}$ are unit vectors along the X and Y axes (parallel and perpendicular, respectively, to the symmetry axis). The grain equation of motion then follows from equations (B1, B2, **??**–**??**) as the following set of coupled differential equations:

$$\begin{aligned} \frac{dX}{dt} &= U \qquad \frac{dY}{dt} = V \\ \frac{dU}{dt} &= \frac{1}{2}\left[X\left(X^2+Y^2\right)^{-3/2} - \alpha_{\text{drag}}^2 D_1\,(U - U_1) \right] \\ \frac{dV}{dt} &= \frac{1}{2}\left[Y\left(X^2+Y^2\right)^{-3/2} - \alpha_{\text{drag}}^2 D_1\,(V - V_1) \right], \end{aligned} \tag{C3}$$

where (U_1, V_1) are the components of the gas velocity (assumed fixed), given by

$$(U_1, V_1) = \begin{cases} \text{parallel stream} & (-1, 0) \\ \text{divergent stream} & \left(\dfrac{X - \mu^{-1}}{R_1}, \dfrac{Y}{R_1} \right), \end{cases} \tag{C4}$$

where

$$R_1 = \left((X - \mu^{-1})^2 + Y^2 \right)^{1/2} \tag{C5}$$

is the distance from the second source, located at $(X, Y) = (\mu^{-1}, 0)$. The dimensionless gas density, D_1, normalized by the value at $(X, Y) = (1, 0)$, is

$$D_1 = \begin{cases} \text{parallel stream} & 1 \\ \text{divergent stream} & \dfrac{(\mu^{-1} - 1)^2}{R_1^2} \end{cases} . \tag{C6}$$

Equations (C3) are integrated using the python wrapper `scipy.integrate.odeint` to the Fortran ODEPACK library (Hindmarsh 1983; Jones et al. 2018), with results shown in Figure **??** for parallel-stream cases and Figure C1 for divergent-stream cases.

APPENDIX D: FURTHER DETAILS ON IONIZATION FRONT TRAPPING

This appendix will probably be dropped from the paper. It contains details of the derivation of the ionization front trapping that I now think are too verbose to be included, given that this is not the main point of the paper. They are collected here for completeness.

We wish to calculate whether the star is capable of photoionizing the entire bow shock shell, or whether the ionization front will be trapped within it. The number of hydrogen recombinations[25] per unit time per unit area in a fully ionized shell is

$$\mathcal{R} = \alpha_{\rm B} n_{\rm sh}^2 h_{\rm sh} , \tag{D1}$$

while the flux of hydrogen-ionizing photons ($h\nu > 13.6\,\mathrm{eV}$) incident on the inner edge of the shell is

$$\mathcal{F} = \frac{S}{4\pi R_0^2} , \tag{D2}$$

where S is the ionizing photon luminosity of the star. Any shell with $\mathcal{R} > \mathcal{F}$ cannot be entirely photoionized by the star, and so must have trapped the ionization front. The column density of the shocked shell can be found, for example, from equations (10) and (12) of Wilkin (1996) in the limit $v_\infty/V \to 0$ (Wilkin's parameter α) and $\theta \to 0$. This yields

$$n_{\rm sh} h_{\rm sh} = \tfrac{3}{4} n R_0 . \tag{D3}$$

Assuming strong cooling behind the shock,[26] the shell density is $n_{\rm sh} = \mathcal{M}_0^2 n$, where $\mathcal{M}_0 = v_\infty / c_{\rm s}$ is the isothermal Mach number of the external stream.[27] Putting these together with equations (3) and (9), one finds that $\mathcal{R} > \mathcal{F}$ implies

$$x^3 \tau_* > \frac{4 S c c_{\rm s} \bar{m}^2 \kappa}{3 \alpha L} . \tag{D4}$$

From equation (11), it can be seen that x depends on the external stream parameters, n, v_∞ only via τ_*, and so equation (24) is a condition for τ_*. In the radiation bow shock case, $x = (1 + \eta)^{1/2}$, and the condition can be written:

$$\tau_* > 145.0 \frac{S_{49} T_4^{1.7} \kappa_{600}}{L_4 (1 + \eta)^{3/2}} , \tag{D5}$$

where

$$S_{49} = S / \left(10^{49}\ \mathrm{s^{-1}}\right) .$$

Numerical values of S_{49} for our three example stars are given in Table 1. In the radiation bow wave case, $x = 2\tau_*$, and the condition can be written:

$$\tau_* > \left(18.1 \frac{S_{49} T_4^{1.7} \kappa_{600}}{L_4} \right)^{1/4} , \tag{D6}$$

$\tau_* \sim n^{1/2} / v_\infty$ This simple criterion is shown by the dark red line in Figure 2. If $n/v_{10}^2 > 1000$ to 5000, depending only weakly on the stellar parameters, then the outer parts of the shocked shell are neutral, instead of ionized.

Assuming photoionization equilibrium, the hydrogen photoabsorption optical depth of the shell is

$$\tau_{\rm gas} = -\ln(1 - \mathcal{R}/\mathcal{F}) , \tag{D7}$$

so long as $\mathcal{R} < \mathcal{F}$.

We will assume a typical photoionized temperature of 8000 K, so that $c_{\rm s} \approx 10\,\mathrm{km\,s^{-1}}$ and $M_0 = v_{10}$, yielding

$$\tau_{\rm gas} = -\ln\left(1 - 8.42 \times 10^{-6}\, v_{10}^2 n^2 R_{0,\rm pc}^3 S_{49}^{-1}\right) , \tag{D8}$$

where

$$R_{0,\rm pc} = R_0 / (1\ \mathrm{pc})$$

The dust opacity is approximately constant at FUV to EUV wavelengths, so the dust optical depth of the shocked shell to ionizing photons follows from equations (8) and (22) as $\tau_{\rm d} = \frac{3}{8}\tau$.

The hydrogen ionization fraction, y, at the outer edge of the shocked shell then follows as

$$\frac{y^2}{1 - y} = \frac{\sigma \mathcal{F}}{\alpha_{\rm B} n} e^{-(\tau_{\rm d} + \tau_{\rm gas})} , \tag{D9}$$

where σ is the effective hydrogen photoionization cross section, averaged over the local ionizing spectrum. Since the frequency-dependent cross section, $\sigma_\nu \sim \nu^{-3}$, is strongly peaked at the threshold, the local EUV spectrum becomes harder with increasing $\tau_{\rm gas}$, as the lower frequency photons are selectively absorbed,[28] leading to a reduction in the effective σ. An approximate fit to the results in Appendix A of Henney et al. (2005) is

$$\sigma = 0.5 \sigma_0 e^{-\tau_{\rm gas}/3} \tag{D10}$$

where $\sigma_0 = 6 \times 10^{-18}\ \mathrm{cm^2}$ is the threshold cross-section. Although this was derived for a particular ionizing spectrum (40 000 K black body), we adopt it for all our hot stars.

[25] The diffuse field is treated in the on-the-spot approximation, assuming all emitted Lyman continuum photons are immediately re-absorbed locally, so the case B recombination co-efficient, $\alpha_{\rm B} = 2.6 \times 10^{-13}\, T_4^{-0.7}\ \mathrm{cm^3\,s^{-1}}$, is used, where $T_4 = T/10^4$ K.

[26] This is shown to be justified in § 2.1.4.

[27] The sound speed depends on the temperature and hydrogen and helium ionization fractions, y and $y_{\rm He}$ as $c_{\rm s}^2 = (1 + y + z_{\rm He} y_{\rm He})(kT/\bar{m})$, where $z_{\rm He}$ is the helium nucleon abundance by number relative to hydrogen and $k = 1.380\,650\,3 \times 10^{-16}\ \mathrm{erg\,K^{-1}}$ is Boltzmann's constant. We assume $y = 1$, $y_{\rm He} = 0.5$, $z_{\rm He} = 0.09$, so that $c_{\rm s} = 11.4\, T_4^{1/2}\ \mathrm{km\,s^{-1}}$.

This paper has been typeset from a TEX/LATEX file prepared by the author.

[28]